Biogeosciences Discuss., 10, 8505–8559, 2013
www.biogeosciences-discuss.net/10/8505/2013/
doi:10.5194/bgd-10-8505-2013
© Author(s) 2013. CC Attribution 3.0 License.

Biogeosciences Discussions
Open Access

This discussion paper is/has been under review for the journal Biogeosciences (BG).
Please refer to the corresponding final paper in BG if available.

The iron budget in ocean surface waters in the 20th and 21st centuries: projections by the Community Earth System Model version 1

K. Misumi[1], K. Lindsay[2], J. K. Moore[3], S. C. Doney[4], F. O. Bryan[2], D. Tsumune[1], and Y. Yoshida[1]

[1]Environmental Science Research Laboratory, Central Research Institute of Electric Power Industry, 1646 Abiko, Abiko, Chiba 270-1194, Japan
[2]Climate and Global Dynamics Division, National Center for Atmospheric Research, P.O. Box 3000, Boulder, CO 80307-3000, USA
[3]Department of Earth System Science, University of California at Irvine, 3214 Croul Hall, Irvine, CA 92697-3100, USA
[4]Department of Marine Chemistry and Geochemistry, Woods Hole Oceanographic Institution, 266 Woods Hole Rd., MS# 25, Woods Hole, MA 02543-1050, USA

Received: 24 April 2013 – Accepted: 8 May 2013 – Published: 22 May 2013

Correspondence to: K. Misumi (misumi@criepi.denken.or.jp)

Published by Copernicus Publications on behalf of the European Geosciences Union.

Abstract

We investigated the simulated iron budget in ocean surface waters in the 1990s and 2090s using the Community Earth System Model version 1 and the Representative Concentration Pathway 8.5 future CO_2 emission scenario. We assumed that exogenous iron inputs did not change during the whole simulation period; thus, iron budget changes were attributed solely to changes in ocean circulation and mixing in response to projected global warming. The model simulated the major features of ocean circulation and dissolved iron distribution for the present climate reasonably well. Detailed iron budget analysis revealed that roughly 70 % of the iron supplied to surface waters in high-nutrient, low-chlorophyll (HNLC) regions is contributed by ocean circulation and mixing processes, but the dominant supply mechanism differed in each HNLC region: vertical mixing in the Southern Ocean, upwelling in the eastern equatorial Pacific, and deposition of iron-bearing dust in the subarctic North Pacific. In the 2090s, our model projected an increased iron supply to HNLC surface waters, even though enhanced stratification was predicted to reduce iron entrainment from deeper waters. This unexpected result could be attributed largely to changes in the meridional overturning and gyre-scale circulations that intensified the advective supply of iron to surface waters, especially in the eastern equatorial Pacific. The simulated primary and export productions in the 2090s decreased globally by 6 % and 13 %, respectively, whereas in the HNLC regions, they increased by 11 % and 6 %, respectively. Roughly half of the elevated production could be attributed to the intensified iron supply. The projected ocean circulation and mixing changes are consistent with recent observations of responses to the warming climate and with other Coupled Model Intercomparison Project model projections. We conclude that future ocean circulation and mixing changes will likely elevate the iron supply to HNLC surface waters and will potentially buffer future reductions in ocean productivity. External inputs of iron to the oceans are likely to be modified with climate change. Future work must incorporate robust estimates of these processes affecting the marine iron cycle.

BGD
10, 8505–8559, 2013

1 Introduction

Iron is an essential nutrient for marine phytoplankton growth and limits primary production in the three major high-nutrient low-chlorophyll (HNLC) regions of the world's oceans, namely, the Southern Ocean, the eastern equatorial Pacific, and the subarctic North Pacific (Martin and Fitzwater, 1988; Martin et al., 1990, 1994). To reduce the uncertainties of climate projections, it is essential to understand iron cycling in the present ocean and to evaluate changes in response to global warming.

The iron budget in ocean surface waters is determined by a combination of exogenous inputs and ocean physical and biogeochemical processes (e.g., Fung et al., 2000). Various processes are responsible for the exogenous inputs: deposition of iron-bearing dust (Duce and Tindale, 1991; Tegen and Fung, 1994; Mahowald et al., 1999; Jickells et al., 2005); reduction and resuspension of sedimentary iron (Johnson et al., 1999; Elrod et al., 2004; Moore et al., 2004; Lam et al., 2006; Nishioka et al., 2007; Lam and Bishop, 2008; Moore and Braucher, 2008; Misumi et al., 2011); and fluvial and hydrothermal inputs (Wetz et al., 2006; Tagliabue et al., 2010; Klunder et al., 2011; Nishioka et al., 2013). Most sedimentary and hydrothermal iron is supplied from continental margins and the ocean abyss to open ocean surface waters by ocean physical processes. Although dissolved iron is considered to be bound and stabilized by organic ligands (Gledhill and van den Berg, 1994; Rue and Bruland, 1995; van den Berg, 1995), uncomplexed iron precipitates rapidly in seawater because of the low solubility of thermodynamically stable Fe(III) (Liu and Millero, 1999). Therefore, favorable ocean bathymetry, circulation, or mixing conditions are required for iron to be transported from sedimentary or hydrothermal sources to surface waters of the open ocean; such conditions may occur, for example, downstream of islands (Blain et al., 2001) or where ocean currents flow swiftly (de Baar et al., 1995; Mackey et al., 2002; Slemons et al., 2009; Misumi et al., 2011). Riverine iron inputs are potentially an important iron source, but most iron in rivers is likely to flocculate and be precipitated in estuaries, because seawater cations neutralize the negatively charged iron-bearing colloids (Boyle et al.,

BGD
10, 8505–8559, 2013

1977). Iron in surface waters is utilized by phytoplankton and is also subject to particle scavenging; it is recycled in the euphotic layer, and a part of the iron is exported to deeper waters as sinking particles. A fraction of the exported iron is then remineralized or desorbed from sinking particles and resupplied to surface waters by upwelling and mixing. In the climatological mean state, iron supplied by dust deposition and by ocean physical processes is balanced by iron removal via biogeochemical processes.

In the HNLC regions, ocean physical processes play an important role in supplying new iron (not regenerated within the euphotic layer) to surface waters where dust deposition is small owing to geographic distance from continental land masses. For example, in the Southern Ocean, ocean physical processes are considered to supply more iron than dust deposition (de Baar et al., 1995; Coale et al., 1996; Fung et al., 2000; Boyd and Ellwood 2010). Physical processes that may contribute to the supply of new iron include upwelling (de Baar et al., 1995), vertical diffusive flux (Boyd et al., 2005), horizontal advection (Ellwood et al., 2008; Sedwick et al., 2008; Bowie et al., 2009), the interaction between bathymetry and currents (Blain et al., 2007; Sokolov et al., 2007), and mesoscale eddies and cross-frontal mixing (Kahru et al., 2007). In addition, the melting of sea ice and icebergs also can supply or redistribute iron in surface waters (Smith et al., 2007; Lannuzel et al., 2008; Lancelot et al., 2009). Similarly, in the eastern equatorial Pacific, ocean physical processes account for most of the supply of new iron to surface waters (Coale et al., 1996; Fung et al., 2000). The iron in this region derives from sediments around Papua New Guinea and is transported eastward via the equatorial undercurrent (EUC) and then supplied to surface waters by upwelling (Mackey et al., 2002; Slemons et al., 2010; Kaupp et al., 2011). The amount of iron supplied is thus sensitive to circulation changes in the western equatorial Pacific. Ryan et al. (2006) suggested that the amount of iron transported is linked to the occurrence of El Niño events, because El Niño events regulate the intensity of the New Guinea Coastal Undercurrent (NGCU), which is the primary source of iron-enriched waters to the EUC. In the subarctic North Pacific, by contrast, dust deposition is considered to be the dominant source of iron to surface waters (de Baar et al., 1995; Fung

BGD
10, 8505–8559, 2013

et al., 2000). Recent studies, however, have suggested that iron derived from continental margin sediments may also play an important role in the iron budget in this region (Lam et al., 2006, 2008; Nishioka et al., 2007, 2011; Moore and Braucher 2008; Misumi et al., 2011).

Various observational and modeling studies have projected changes in meridional overturning and gyre-scale circulations, water column stratification, and eddy activities in response to global warming. Such changes are likely to alter the iron budget in HNLC surface waters. The Intergovernmental Panel on Climate Change (IPCC) Fourth Assessment Report (AR4) concluded that warmer climatic conditions enhance surface water stratification (Meehl et al., 2007), which can reduce the amount of iron supplied by vertical mixing (Steinacher et al., 2010). Westerly winds over the Southern Ocean are projected to intensify (Meijers et al., 2012), and most climate models show that the mean flow of the meridional overturning circulation is enhanced by intensified westerly winds (Hallberg and Gnanadesikan, 2006; Meredith and Hogg, 2006; Hogg et al., 2008; Screen et al., 2009; Spence et al., 2010; Farneti et al., 2010; Gent and Danabasoglu, 2011). Several studies have shown that increased radiative forcing causes southern subtropical gyres to spin up and shift southward (Beal et al., 2011; Meijers et al., 2012). In the western equatorial Pacific, Coupled Model Intercomparison Project (CMIP) phase 3 (CMIP3) models have projected a substantial decrease of the South Equatorial Counter Current (SECC) flow (Ganachaud et al., 2012). One high-resolution ocean model has projected that the flow of the Kuroshio Current will accelerate under global warming (Sakamoto et al., 2005). How these circulation changes will affect the iron budget in HNLC surface waters is still uncertain.

In this study, we used a CMIP phase 5 (CMIP5) model to investigate the iron budget in ocean surface waters, with a particular focus on HNLC surface waters. We evaluate future iron cycling changes and their impact on ocean productivity under one global warming scenario on the basis of our understanding of the iron budget of the present ocean. We show that the simulated iron budget of the surface waters for the 1990s is consistent with previous estimations. The model projections show that in the 2090s

BGD
10, 8505–8559, 2013

changes in ocean circulation and mixing will intensify the amount of iron supplied to HNLC surface waters, despite enhanced stratification of those waters. Thus, future ocean iron cycle changes will potentially enhance ocean productivity and thus partly compensate for decreases in ocean productivity caused by reduced macronutrient entrainment.

In Sect. 2, we describe the climate model used and the analytical method. We present the simulated results in Sect. 3. In Sect. 4, we compare the simulated iron budget for the 1990s with other estimations and discuss future ocean iron budget changes in HNLC surface waters and their potential impact on ocean productivity. We summarize our conclusions in the final section.

2 Model and methods

2.1 Model

We used the Community Earth System Model (CESM1; Hurrell et al., 2013; available online at http://www.cesm.ucar.edu), a CMIP5 model developed for contributing to the IPCC Fifth Assessment Report (AR5). We used the CESM1-BGC model configuration (Lindsay et al., 2013); this configuration is mostly the same as the default configuration of the previously released Community Climate System Model version 4 (CCSM4; Gent et al., 2011). Different from the default CCSM4 configuration, the CESM1-BGC configuration includes a marine ecosystem module, three-dimensional atmospheric CO_2 tracers, and interactive coupling of the oceanic components to each other and to the land model. In addition, the CESM1-BGC configuration calculates the absorption of short-wave radiation in the upper ocean using the simulated chlorophyll field, whereas the default CCSM4 configuration calculates it by using a climatology based on satellite observations. The simulated physical states differ little, however, between the CESM1-BGC and CCSM4 configurations; thus, we refer readers to recently published CCSM4 papers for details (e.g., Gent et al., 2011; Danabasoglu et al., 2012).

BGD
10, 8505–8559, 2013

CESM1 consists of four major component models, the atmospheric, land, ocean, and sea-ice components, that are coupled interactively by a flux coupler (CPL7; Craig et al., 2011). The atmospheric and land components are the Community Atmospheric Model version 4 (CAM4; Neale et al., 2013) and Community Land Model version 4 (Lawrence et al., 2012), respectively. Both models adopt a uniform horizontal resolution of $1.25^\circ \times 0.9^\circ$, and the CAM4 has 26 vertical layers. The ocean component is the Parallel Ocean Program version 2 (POP2; Smith et al., 2010; Danabasoglu et al., 2012), and the sea-ice component is the Community Ice Code version 4 (Hunke and Lipscomb, 2008; Holland et al., 2012). These components adopt a non-uniform horizontal grid on which the north pole is displaced onto Greenland. This grid has a zonal resolution of 1.125° and a meridional resolution that varies from 0.27° around the equator, and the maximum resolution is about 0.64° located in the northwestern Pacific. The POP2 has 60 vertical levels, which are 10 m thick in the upper 150 m; below 150 m their thickness increases with depth.

The CESM1-BGC configuration includes the Biogeochemical Elemental Cycling (BEC) model (Moore et al., 2004, 2013) as the marine ecosystem module. This module simulates four phytoplankton functional type classes (pico/nanoplankton, coccolithophores, diatoms, and diazotrophs), one zooplankton class, five nutrients (dissolved nitrate, ammonia, phosphorus, iron, and silicate), inorganic carbon system geochemistry, and oxygen cycling. The model skill in simulating ecology and biogeochemistry, including iron cycling, has been documented previously (Moore et al., 2004, 2013; Moore and Braucher, 2008; Doney et al., 2009a,b; Misumi et al., 2011, 2013a,b).

The BEC model considers two external iron sources: aeolian dust (Luo et al., 2003) and seafloor sediments (Moore and Braucher, 2008). Aeolian dust is assumed to contain a constant fraction of iron (3.5 wt %), and a small fraction, 2 %, of the dust iron is assumed to dissolve instantaneously at the sea surface. The model also considers the dissolution of dust iron as it sinks in the water column (Moore and Braucher, 2008). BEC uses the monthly mean climatology of aeolian dust and the annual mean climatology of the sedimentary iron flux. We assumed that these fluxes did not change

BGD
10, 8505–8559, 2013

throughout the simulation period (from 1850 to 2100). Riverine and hydrothermal iron inputs and iron incorporated in sea ice or icebergs are not considered in this version of the BEC model.

In this study, we base our findings on results from two simulation experiments, a 20th century simulation and a 21st century simulation, using prescribed anthropogenic CO_2 emissions. Lindsay et al. (2013) have documented the simulation for 1850 to 2005, called the 20C PROG experiment, and have described the initial conditions, spinup procedure, and transient forcing for the 20th century simulation. For the simulation from 2005 to 2100, the model was run with the Representative Concentration Pathways 8.5 (RCP8.5) CO_2 emission scenario (Moss et al., 2010; van Vuuren et al., 2010). This scenario assumes a nominal anthropogenic forcing of $8.5\,W\,m^{-2}$ by 2100. The simulated data are available online at the CMIP5 website (http://cmip-pcmdi.llnl.gov/cmip5/). Moore et al. (2013) and Long et al. (2013) have documented the model skill in simulating ecology and biogeochemical tracers averaged over the 1990s in comparison with observational datasets. In this paper, we focus on the ocean iron budget averaged over two periods, the 1990s and the 2090s. This work complements the broader ecosystem analysis for these two time periods by Moore et al. (2013).

2.2 Iron budget analysis

The BEC model calculates the net dissolved iron tendency (TEND) or time rate of change of the dissolved iron concentration in each grid box as the sum of the following terms

$$\mathrm{TEND} = \mathrm{PHYS} + \mathrm{BGC} + \mathrm{FRC} = (\mathrm{ADV} + \mathrm{MIX} + \mathrm{MIXn}) + \mathrm{BGC} + \mathrm{FRC}, \quad (1)$$

where the terms represent simulated dissolved iron tendencies due to advection by large-scale flows (ADV), isopycnal and parameterized eddy mixing (MIX), non-local convective mixing (MIXn), biogeochemical processes (BGC), and external forcings (FRC). The ADV and MIX terms can be subdivided into horizontal (ADVh and MIXh)

BGD
10, 8505–8559, 2013

and vertical (ADVv and MIXv) components. PHYS, that is, the sum of the ADV, MIX, and MIXn terms, represents the net ocean physical processes. The difference between the 2090s and the 1990s is denoted by putting a "δ" before the term name. In this study, we consider the iron budget in the upper 100 m of the ocean, unless otherwise noted.

For each specific region, we define the iron budget amplitude (Amp) as follows:

$$\mathrm{Amp} \equiv \frac{1}{2}\sum_i \left| \int \mathrm{terms}_i \mathrm{d}V \right|, \tag{2}$$

where terms_i represents the individual iron budget terms (see Sect. 3.3), dV represents a specific region. The Amp ratio (rAmp) is defined as follows:

$$\mathrm{rAmp} \equiv \frac{\delta\mathrm{Amp}}{\mathrm{Amp}_{1990\mathrm{s}}}, \tag{3}$$

where $\mathrm{Amp}_{1990\mathrm{s}}$ represents the decadal average of Amp values in the 1990s.

We further decompose the difference in the advection term between the 2090s and the 1990s (δADV) to investigate the mechanism of the change. The advection term can be written as the iron flux convergence:

$$\mathrm{ADV} = -\nabla\cdot(\boldsymbol{v}\,\mathrm{Fe}), \tag{4}$$

where $\boldsymbol{v}$ represents three-dimensional velocity and Fe represents the dissolved iron concentration. The advection term in the 1990s can be written as

$$\mathrm{ADV}_{1990\mathrm{s}} = -\nabla\cdot\langle[\boldsymbol{v}\,\mathrm{Fe}]_{1990\mathrm{s}}\rangle = -\nabla\cdot\langle[\boldsymbol{v}]_{1990\mathrm{s}}[\mathrm{Fe}]_{1990\mathrm{s}}\rangle - \nabla\cdot\left\langle\left[\boldsymbol{v}'\mathrm{Fe}'\right]_{1990\mathrm{s}}\right\rangle, \tag{5}$$

where the box bracket $[X]_{\mathrm{decade}}$ is decadal monthly mean, the angle brackets $\langle X\rangle$ is annual mean and the prime superscript X' denotes deviation from the decadal monthly mean for the monthly mean output of a variable X. The difference in the advection term

BGD
10, 8505–8559, 2013

between the 2090s and the 1990s is thus,

$$\begin{aligned}\delta\mathrm{ADV} &= -\nabla\cdot\langle[\boldsymbol{v}]_{2090\mathrm{s}}[\mathrm{Fe}]_{2090\mathrm{s}}\rangle + \nabla\cdot\langle[\boldsymbol{v}]_{1990\mathrm{s}}[\mathrm{Fe}]_{1990\mathrm{s}}\rangle - \nabla\cdot\left\langle\left[\boldsymbol{v}'\mathrm{Fe}'\right]_{2090\mathrm{s}}\right\rangle \\ &\quad + \nabla\cdot\left\langle\left[\boldsymbol{v}'\mathrm{Fe}'\right]_{1990\mathrm{s}}\right\rangle \\ &\approx -\nabla\cdot\langle[\boldsymbol{v}]_{2090\mathrm{s}}[\mathrm{Fe}]_{2090\mathrm{s}}\rangle + \nabla\cdot\langle[\boldsymbol{v}]_{1990\mathrm{s}}[\mathrm{Fe}]_{1990\mathrm{s}}\rangle .\end{aligned} \tag{6}$$

The sum of the covariance terms was very small in regions where this analysis is applied; thus we neglect them. The first term of the last line of Eq. (6) can be rewritten as,

$$\begin{aligned}\langle[\boldsymbol{v}]_{2090\mathrm{s}}[\mathrm{Fe}]_{2090\mathrm{s}}\rangle &= \langle([\boldsymbol{v}]_{1990\mathrm{s}} + \delta[\boldsymbol{v}])([\mathrm{Fe}]_{1990\mathrm{s}} + \delta[\mathrm{Fe}])\rangle \\ &= \langle[\boldsymbol{v}]_{1990\mathrm{s}}[\mathrm{Fe}]_{1990\mathrm{s}}\rangle + \langle\delta[\boldsymbol{v}][\mathrm{Fe}]_{1990\mathrm{s}}\rangle + \langle[\boldsymbol{v}]_{1990\mathrm{s}}\delta[\mathrm{Fe}]\rangle \\ &\quad + \langle\delta[\boldsymbol{v}]\delta[\mathrm{Fe}]\rangle .\end{aligned} \tag{7}$$

By substituting Eq. (7) into Eq. (6), we can decompose δADV into three terms,

$$\delta\mathrm{ADV} \approx -\nabla\cdot\langle\delta[\boldsymbol{v}][\mathrm{Fe}]_{1990\mathrm{s}}\rangle - \nabla\cdot\langle[\boldsymbol{v}]_{1990\mathrm{s}}\delta[\mathrm{Fe}]\rangle - \nabla\cdot\langle\delta[\boldsymbol{v}]\delta[\mathrm{Fe}]\rangle . \tag{8}$$

The first and second terms on the right-hand side are interpreted as the advective flux convergence change due to velocity and iron distribution changes, respectively; the last term is non-linear. By evaluating the relative importance of these terms we can elucidate which processes dominantly cause the net advective flux convergence change. In the following, we denote the horizontal flux convergence as $-\nabla\cdot(\boldsymbol{u}\mathrm{Fe})$ and the vertical flux convergence as $-\partial(w\mathrm{Fe})/\partial z$, respectively.

We also decompose the mixing term (MIX) into eddy ($\mathrm{MIX}_{\mathrm{eddy}}$) and residual ($\mathrm{MIX}_{\mathrm{resi}}$) components:

$$\mathrm{MIX} = \mathrm{MIX}_{\mathrm{eddy}} + \mathrm{MIX}_{\mathrm{resi}} . \tag{9}$$

The $\mathrm{MIX}_{\mathrm{eddy}}$ component is calculated by using the parameterization of Gent and McWilliams (1990) for the quasi-adiabatic ocean interior. Near the surface boundary, the effects of the diabatic mesoscale fluxes within the surface diabatic layer are

BGD
10, 8505–8559, 2013

calculated with the simplified near-boundary eddy flux parameterization of Ferrari et al. (2008), as implemented by Danabasoglu et al. (2008). The restratification effects of finite-amplitude, submesoscale mixed-layer eddies are also included by use of the mixed-layer eddy parameterization of Fox-Kemper et al. (2008) as implemented by Fox-Kemper et al. (2011). The MIX_{resi} component is obtained by subtracting MIX_{eddy} from MIX. Note that the MIX_{resi} component does not include non-local convective mixing (MIXn), which is treated separately from the MIX term (see Eq. 1). The MIXn term is calculated by the *K*-Profile Parameterization (Large et al., 1994; as modified by Danabasoglu et al., 2006).

3 Results

3.1 Overview of the simulated physical and biogeochemical fields

The atmospheric CO_2 concentration in the 1990s was simulated to be 376 ppm (Fig. 1a), a value somewhat higher than the observed concentration in the 1990s (359.82 ppm; Ed Dlugokencky and Pieter Tans, NOAA/ESRL http://www.esrl.noaa.gov/gmd/ccgg/trends/). The simulated concentration increased to 1076 ppm by the 2090s. The globally averaged simulated sea surface temperature increased from 18.7 °C to 21.7 °C from the 1990s to the 2090s (Fig. 1b). The simulated primary and export productions decreased from 56.1 to 52.9 $Gt\,C\,yr^{-1}$ and from 8.07 to 7.00 $Gt\,C\,yr^{-1}$ from the 1990s to the 2090s, respectively (Fig. 1c and d; Table 1). The simulated marine primary and export productions in the 1990s fell within the range of previous estimates (36.5–67 $Gt\,C\,yr^{-1}$ for primary production; Longhurst et al., 1995; Antoine et al., 1996; Behrenfeld and Falkowski, 1997; Behrenfold et al., 2005; $10 \pm 3\,Gt\,C\,yr^{-1}$ for export production; Sarmiento and Gruber, 2006). Although the globally averaged surface nitrate concentration was projected to decrease from 7.58 to 6.27 µM from the 1990s to the 2090s (Fig. 1e), the surface dissolved iron concentration was projected to increase from 0.69 to 0.75 nM (Fig. 1f).

BGD
10, 8505–8559, 2013

The model reproduced known basin-scale barotropic (vertically integrated) stream function (BSF) distributions well, but the results for the 1990s showed some biases in detail (Fig. 2a). The simulated Antarctic Circumpolar Current (ACC) transport through the Drake Passage was 170 Sv, roughly 25 % larger than the observational estimate (137 ± 8 Sv) (Cunningham et al., 2003). The simulated South Atlantic subtropical gyre transport was up to 58 Sv, which is more than double observed values (Large and Danabasoglu, 2006; Danabasoglu et al., 2012). Simulated maximum transport of the Kuroshio (58 Sv) was consistent with an estimate based on altimeter data (57 Sv, including local recirculation; Imawaki et al., 2001), but the current is simulated to extend somewhat too far northward, as is typical of low-resolution ocean models (e.g., Hasumi et al., 2010). The simulated transport of the East Kamchatka Current (11 Sv), the western boundary current in the subarctic North Pacific, is lower than the estimated geostrophic transport relative to the sea bottom (13–24 Sv, Talley and Nagata, 1995), a result that implies that the simulated subarctic gyre transport in the North Pacific is weaker than the actual transport.

In the 2090s, the overall patterns of the simulated BSF distributions are similar to those in the 1990s (Fig. 2b), but with moderate differences in some regions (Fig. 2c). In the Southern Hemisphere oceans south of 20° S, the alternation of positive, negative, and positive values in the meridional direction imply that the southern subtropical gyres and the ACC shift southward. For example, the zonal average of the zero-contour latitude of the BSF in the Southern Ocean was projected to shift from 44.8° S to 46.4° S between the 1990s and the 2090s. The South Atlantic subtropical gyre transport was projected to increase by 40 % to 80 Sv in the 2090s, whereas the subtropical gyre in the North Pacific was projected to weaken in the 2090s. The western subarctic gyre transport in the North Pacific was projected to increase by roughly 30 % to 14 Sv in the 2090s, but the Alaskan Gyre was projected to be somewhat weaker.

The model simulated large-scale patterns of primary and export production rates compare reasonably well with satellite-based estimations (Fig. 3a and c; cf., Sarmiento and Gruber, 2006), though the model somewhat overestimated those rates in the sub-

BGD
10, 8505–8559, 2013

tropical oceans and underestimated them in the subarctic North Pacific. The simulated surface nitrate concentrations were also higher in the subtropical oceans and lower in the subarctic North Pacific (Fig. 3e; see also Moore et al., 2013). Point-by-point comparison of surface dissolved iron concentrations between field observations and simulated data showed large dispersion (Fig. 4b), but the basin-scale distribution was simulated reasonably well (Fig. 4c). The model successfully simulated the known HNLC regions (i.e., iron-limited areas for phytoplankton growth) in the Southern Ocean, the eastern equatorial Pacific, and the subarctic North Pacific, though it underestimated the areal extent of the subarctic North Pacific HNLC region (Fig. 5; see also Moore et al., 2013).

Although the globally integrated primary and export production rates decreased in the RCP8.5 simulation (Fig. 1c and d), in iron-limited areas in particular, these rates were simulated to increase in the 2090s (Fig. 3b and d). This result implies that changes in iron cycling fuel production in HNLC regions. Moore et al. (2013) has briefly described this response, and we discuss it in greater detail in Sect. 4. Surface nitrate concentrations were projected to decrease almost everywhere globally in the 2090s as a result of decreased entrainment from deeper waters due mainly to enhanced stratification (Fig. 3f; see also Moore et al., 2013). The projected reduction of surface nitrate concentrations in nitrate-limited areas also led to a decrease in the biological uptake of iron and particle scavenging and resulted in increased surface dissolved iron concentrations in non-HNLC regions in the 2090s (Fig. 3h). The areal extent of the iron-limited areas was also projected to shrink by the 2090s (Fig. 5).

3.2 Simulated oceanic iron budget in global surface waters

The values for the total TEND term (see Sect. 2.2) in the 1990s were very small compared with the values of its individual component terms (Fig. 6), a result that implies that surface water iron concentrations are in a quasi-steady state. Simulated FRC values were positive in the global ocean, and they were especially large in the equatorial Atlantic, the northern Indian Ocean, and near coasts (Fig. 6g) because of iron supplied

BGD
10, 8505–8559, 2013

from aeolian dust and continental margin sediments. Simulated PHYS values, which represent iron supplied via three-dimensional advection and mixing, were positive in most regions (Fig. 6c). Negative PHYS values mean that large external iron inputs exceed the amount of locally consumed iron, which is represented by the BGC term, and that the surplus iron is exported to adjacent areas or to deeper waters. Negative BGC values mean that iron is exported from surface waters by the biological pump and by particle scavenging (Fig. 6e).

Globally in the 1990s, the total amount of iron supplied to the upper 100 m accounted for by the FRC term was 40.8 Gmol yr^{-1}: 8.29 Gmol yr^{-1} from aeolian dust and 32.5 Gmol yr^{-1} from sediments (Table 2). The PHYS term accounted for only 4.09 Gmol yr^{-1}, roughly 10 % of total iron supply to the upper 100 m. Although the global integral was small, ocean physical processes were considered to play a key role in the surface iron budget because the PHYS term values exceeded the FRC term values in 73 % of the global ocean areas (Figs 6c and 6g). The decomposition of the PHYS term shows that convective mixing was the most important physical process affecting the supply of iron to surface waters (60 % of the total). The BGC term accounted for the removal of 44.9 Gmol yr^{-1} of iron from surface waters, an amount that balances the total iron inputs accounted for by the FRC and PHYS terms. The spatial patterns of the PHYS and BGC term differences are similar to each other but with opposite sign (Fig. 6d and f). At a global scale, the net iron supply accounted for by the PHYS term decreased to 3.83 Gmol yr^{-1} in the 2090s (Table 2).

3.3 Iron supply processes to HNLC surface waters

A detailed examination of the processes associated with supplying iron to HNLC surface waters showed that positive PHYS term values were larger than positive FRC term values in the 1990s in a large part of the area comprising HNLC regions (Fig. 6c and g). This result implies that in these regions the iron supply via ocean physical processes was more important than the supply from external sources. The total iron supply to HNLC surface waters was 2.33 Gmol yr^{-1} in the 1990s, roughly two-thirds of

BGD
10, 8505–8559, 2013

which was accounted for by the PHYS term (1.60 Gmol yr^{-1}; Table 2). Positive δPHYS values in HNLC areas (Fig. 6d) indicate elevated amounts of iron supplied via physical processes in the 2090s compared with the 1990s, whereas the corresponding negative BGC term values indicate intensified export of iron by the biological pump and particle scavenging (Fig. 6f). Although the globally integrated PHYS term decreased in the 2090s, the value integrated over the HNLC areas increased from 1.60 to 1.81 Gmol yr^{-1} (Table 2).

We defined four HNLC regions by dividing the simulated iron-limited areas for diatoms in the 1990s according to latitude (Fig. 5c): higher latitudes of the Southern Ocean (HIGH SO), south of 60° S; lower latitudes of the Southern Ocean (LOW SO), between 30° S and 60° S; the eastern equatorial Pacific (EEQPAC), between 30° S and 30° N; and the subarctic North Pacific (SNPAC), north of 30° N in the Pacific.

3.3.1 Southern Ocean

In HIGH SO in the 1990s, the largest positive values are those of the MIXn term (Fig. 7a); this result indicates that non-local convective mixing is the dominant iron source. External iron inputs (FRC) play only a minor role in HIGH SO. The ADVv and ADVh components, with positive and negative values, respectively, represent the vertical iron supply from deeper waters and lateral iron export to lower latitudes, respectively, by the overturning circulation.

The spatial distribution of each physical component provides a more detailed view of the iron supply processes in this region (Fig. 8). Large positive values of the MIXn term are seen along the coast of Antarctica (Fig. 8e), and they are especially large in the Weddell and Ross seas. Positive values of the ADVv component are distributed over most of HIGH SO, and the corresponding ADVh component values are negative (Fig. 8a and b); together, these terms represent iron transport by the overturning circulation. The negative MIXh component values along the coast of Antarctica and the positive values in offshore regions, along with the offshore-directed iron flux vectors

BGD
10, 8505–8559, 2013

(Fig. 8c), indicate mixing of coastal and open ocean waters and net transport of iron in the offshore direction (Misumi et al., 2011). The signs of the MIXv values (Fig. 8d) are basically determined by the directions of the MIXh vectors (Fig. 8c) and the isopycnal slope (generally upward toward the south in surface waters of the Southern Ocean). In regions where the MIXh vectors point southward (northward), the sign of the MIXv values is generally positive (negative) because of the upward (downward) slope of the isopycnals.

In the 2090s, changes in the iron budget from the 1990s are moderate in HIGH SO (Fig. 7a–c; rAmp= 0.395). The largest change is in the MIXn term, the value of which decreases by more than 60 % from the 1990s. Strong warming and freshening of the surface waters enhance stratification and prevent non-local convective mixing, especially in the Weddell and Ross seas (Fig. 9e). By contrast, the MIXv component value changes from a moderately negative value in the 1990s to a small positive value in the 2090s (Fig. 7a and b); as a result, the largest increase is seen in this difference term (Fig. 7c).

The similar spatial pattern, but with opposite sign, of the change in the values of the MIXv and MIXn components between the 2090s and 1990s along the coast of Antarctica (Fig. 9d and e) implies a linkage between these processes. We examined these processes in the Weddell Sea, where the largest change is seen. Viewed in a zonal cross section (Fig. 10a), the large negative values of the MIXv component in the upper 60 m eastward of the Antarctic Peninsula explain the negative MIXv values averaged over the upper 100 m (Fig. 8d). Annual mean potential density in the section slopes upward toward the Antarctic coast (Fig. 10a) owing to deep winter-time non-local convective mixing near the coast (not shown). The density front results in an eddy-induced flow toward the coast that tends to restratify the surface water and results in large iron fluxes toward the coast and a vertical iron flux divergence near the coast (Fig. 10b). Because the eddy-induced flow transports open ocean waters with lower dissolved iron concentrations toward the coast, the residual component flow transports iron away from the coast (Fig. 10c). In the offshore region, the residual fluxes generally

BGD
10, 8505–8559, 2013

follow the isopycnals (Fig. 10c); as a result, vertical flux divergence (negative MIX_{resi} values) is seen offshore. The fact that the density front near the coast caused by the MIXn term drives the vertical flux divergence in the MIXv term explains the linkage between these components.

In the 2090s, enhanced stratification of the surface waters due to warming and freshening weakens non-local convective mixing and the density front near the coast; as a result, the eddy-induced flow driving the vertical flux divergence in the MIXv component disappears (Fig. 10d–f). Although the enhanced stratification reduces the iron supply to the surface waters by non-local convective mixing, the disappearance of the frontal structure means that local mixing lessens the vertical iron flux divergence, which partly compensates for the decrease in the MIXn term (Fig. 7c).

The larger positive value of the ADVv term in the 2090s compared with the 1990s accounts for the ADVv difference term having the second largest positive value (Fig. 7c). Decomposition of the δADVv term by Eq. (8) shows roughly equal contributions from the $-\partial\langle\delta[w][\mathrm{Fe}]_{1990s}\rangle/\partial z$ and $-\partial\langle[w]_{1990s}\delta[\mathrm{Fe}]\rangle/\partial z$ components (Fig. 11a); thus, the velocity and iron distribution changes are of equal importance. An intensified mean flow of the meridional overturning circulation along with stronger westerly winds over the Southern Ocean in the 2090s (Meehl et al., 2012) likely account for the larger $-\partial\langle\delta[w][\mathrm{Fe}]_{1990s}\rangle/\partial z$ value. In contrast, the larger $-\partial\langle[w]_{1990s}\delta[\mathrm{Fe}]\rangle/\partial z$ value can probably be attributed to a larger vertical concentration gradient caused by the enhanced stratification.

In LOW SO in the 1990s, the FRC term is the largest source of iron to surface waters, accounting for roughly 36 % of the total iron input, and the MIXh, MIXv, and MIXn terms contribute equally to the surface iron supply (Fig. 7d). Because the balance among the terms in the 2090s hardly changes from that in the 1990s (Fig. 7d and e) the rAmp value is low (0.122; Fig. 7f). The largest change is in the value of the ADVh term, which is roughly 0.1 $\mathrm{Gmol\,yr^{-1}}$ larger in the 2090s. Because in the adjacent HIGH SO δADVh indicates an iron export (negative value) of only 0.015 $\mathrm{Gmol\,yr^{-1}}$ (Fig. 7c), the rest of the added iron must come from lower latitudes. The spatial distribution of values of the

BGD
10, 8505–8559, 2013

δADVh term shows negative values at around 40° S (outside of the HNLC region) and positive values downstream in the Atlantic sector of LOW SO (Fig. 9a); this distribution is likely attributable to a southward shift and spinup of the southern subtropical gyres (Fig. 2). In particular, large positive δADVh values are seen in the Atlantic sector of LOW SO (Fig. 9a), where the horizontal flux vectors originate in the west. These results imply that an intensified south Atlantic subtropical gyre will transport more iron to LOW SO in the 2090s. Decomposition of δADVh between 30° W and 30° E in LOW SO with Eq. (7) shows that the contribution from the $-\nabla\cdot\langle\delta[\boldsymbol{u}][\mathrm{Fe}]_{1990\mathrm{s}}\rangle$ component is largest; this means that an intensified mass flux is mainly responsible for the elevated horizontal iron advection in this area.

3.3.2 Eastern equatorial Pacific

In EEQPAC in the 1990s, external iron inputs (FRC) are small (20 %), and most iron is supplied by the ADVv component (65 %), that is, by equatorial upwelling (Fig. 7g). Much of this iron is transported by the EUC and originates in the western equatorial Pacific (Moore et al., 2013). Large vertical iron fluxes from subsurface to surface waters are seen in the eastern equatorial Pacific (Fig. 12g). The vertical flux divergence (negative values) in the subsurface water (Fig. 12g) is supported by the zonal supply of iron (positive values) from the western region (Fig. 12c). A large zonal iron flux divergence at around 150° E (Fig. 12c) corresponds to a large meridional iron flux convergence (Fig. 12e). The simulated horizontal iron transport for the 1990s shows large northward iron fluxes along the coast of Papua New Guinea, where iron inputs from shelf sediments cause the divergence of these fluxes (Fig. 13a and e). The northward fluxes converge at around 150° E in the equatorial region (Fig. 13a); as a result, a large meridional flux convergence is seen at around 150° E (Fig. 12e). Thus, the iron supplied to the eastern equatorial Pacific originates mainly in shelf sediments of Papua New Guinea and is transported via the EUC.

In the 2090s, the simulated SECC (the eastward flow at around 7° S in Fig. 13a) declines; this result is supported by the positive value of the BSF difference off Papua New

BGD
10, 8505–8559, 2013

Guinea (Fig. 2c). The weaker SECC off Papua New Guinea enhances the northward iron flux along the coast. As a result, dissolved iron concentration anomalies are negative and positive in the SECC and along the coast of Papua New Guinea, respectively (Fig. 13b, magenta and green contours, respectively). The elevated zonal dissolved iron concentration gradient results in larger dissolved iron transport mediated by the EUC (Fig. 12d), the result being that the supply of iron to surface waters by equatorial upwelling is larger in the eastern part of the region (Fig. 12h). Decomposition of δADVv in the upper 100 m and δADVh in the 100–300 m depth interval with Eq. (8) shows a large contribution of the concentration difference term $(-\partial\langle[w]_{1990s}\delta[\mathrm{Fe}]\rangle/\partial z$ and $-\nabla\cdot\langle[\boldsymbol{u}]_{1990s}\delta[\mathrm{Fe}]\rangle$; Fig. 11c and d); thus, changes in the dissolved iron distribution drive the enhanced iron supply to surface waters in EEQPAC.

3.3.3 Subarctic North Pacific

In SNPAC in the 1990s, 49 % of the iron supplied to surface waters in the 1990s is explained by the FRC term (Fig. 7j), with a moderate contribution accounted for by the MIXh term (26 %). Because the Kuroshio Current and the Alaskan stream transport iron to the Kuroshio Extension region and along the Aleutian Islands by horizontal advection (Fig. 14a), relatively high dissolved iron concentrations are seen around SNPAC (Fig. 3g); thus, iron is transported to the iron-limited area by lateral mixing (Fig. 14c). The positive ADVv term (Fig. 7j) represents iron transport by Ekman upwelling (Fig. 14b).

The term balance hardly changes in the 2090s (Fig. 7k), and the rAmp value is very small (0.092). The largest change is in the ADVh term. Relatively large iron flux vectors are seen in the region of the western boundary currents in the Bering Sea and the Okhotsk Sea, and the vectors penetrate the iron-limited area (Fig. 15a). Intensified cyclonic gyre circulations in the marginal seas (Fig. 2) probably increase the transport of sedimentary iron to SNPAC.

BGD
10, 8505–8559, 2013

4 Discussion

4.1 Iron budget in surface waters and projected changes under future climate conditions

The simulated surface iron budget for the 1990s is consistent with the findings of previous studies. In our simulation, 8.29 Gmol yr^{-1} of iron from aeolian dust dissolves in the upper 100 m (Table 2); 6.62 Gmol yr^{-1} of this amount dissolves at the ocean surface, and the remaining 1.67 Gmol yr^{-1} dissolves subsequently as the dust particles sink in the upper 100 m. Similarly, Jickells et al. (2005), who compiled recent modeling estimates (Ginoux et al., 2001; Mahowald and Luo, 2003; Tegen et al., 2004), estimated dissolution of 5.72 Gmol yr^{-1} at the ocean surface by assuming 2 % iron solubility. Elrod et al. (2004) estimated the global iron supply from continental margin sediments to be 89 Gmol yr^{-1} based on an assumed global shelf area (0–200 m depth) of 3×10^{13} m^2 for (Menard and Smith, 1966). The sedimentary iron flux used in our simulation (32.5 Gmol yr^{-1}) is similar to the flux estimated by Elrod et al. (2004) if the fact that our analysis applies to the 0–100 m depth range is taken into account. The ocean physical processes simulated in this study supply iron to global surface waters at a rate of 4.09 Gmol yr^{-1} (Table 2), a value that is comparable to previous model estimates of 3.29–3.56 Gmol yr^{-1} (Archer and Johnson, 2000) and 3.65 Gmol yr^{-1} (Aumont et al., 2003). Using observed Fe : NO_3 ratios, vertical velocity simulated by a model, and a simple advection–diffusion equation, Fung et al. (2000) estimated that iron is supplied by ocean physical processes at a rate only about one-sixth (0.7 Gmol yr^{-1}) the size of our estimate. Aumont et al. (2003) discussed the difference between their results and those of Fung et al. (2000) and attributed the low estimate of Fung et al. (2000) to the use of a small vertical diffusivity coefficient of at most 1 cm^2 s^{-1}. We agree with Aumont et al. (2003); in our simulation, the simulated vertical diffusivity due to non-local convective mixing is as high as $O(10)$ cm^2 s^{-1} in regions where deep convection develops, and in our global simulation for the 1990s, the MIXn term accounted for the largest supply (Table 2; 2.47 Gmol yr^{-1}).

BGD
10, 8505–8559, 2013

We found that most iron is supplied to HNLC surface waters via physical processes (roughly 70 % in our simulation; Table 2), the implication being that HNLC surface waters are sensitive to changes in ocean physical processes. The specific processes transporting iron to HNLC surface waters differ from region to region; thus, the impact of future climate change on the surface iron budget is also likely to differ among the individual regions.

In high latitudes of the Southern Ocean, our simulation results indicate that most iron is supplied to surface waters by non-local convective mixing and that direct iron input from external sources plays only a minor role. Enhanced stratification of the surface waters under future climate conditions might therefore be expected to cause a decrease of the iron supply to surface waters. Our simulation, however, showed a possible mechanism that might compensate for this reduction in the iron supply. In our simulation, the cessation of convective mixing weakens the density front and the downward iron export induced by cross-frontal submesoscale eddies, partly compensating for the reduction of the iron supply by convective mixing. In addition, intensified zonal winds over the Southern Ocean in the future climate are predicted to accelerate the mean flow of the meridional overturning circulation; thus, the surface iron supply by vertical advection would be elevated. These results indicate that the net iron supply change may be small in high latitudes of the Southern Ocean even if there is a large reduction in the amount of iron supplied by convective mixing.

The simulated ocean responses in high latitudes of the Southern Ocean to global warming appear to be reasonable when compared to the findings of previous studies. In an analysis based on CMIP3 simulations, IPCC AR4 projected that the Antarctic sea ice cover would shrink and surface stratification would be enhanced in the 21st Century (Meehl et al., 2007). Strengthening winds over the Southern Ocean are seen in observation data (Marshall, 2003) and also in future projections by CMIP5 simulations (Meijers et al., 2012). Various model simulations have predicted intensification of the mean flow of the meridional overturning circulation driven by stronger westerly winds (Hallberg and Gnanadesikan, 2006; Meredith and Hogg, 2006; Hogg et al., 2008; Screen

BGD
10, 8505–8559, 2013

et al., 2009; Spence et al., 2010; Farneti et al., 2010; Gent and Danabasoglu, 2011). Thus, we conclude that the simulated iron cycle changes in the high latitudes of the Southern Ocean are reasonable, at least qualitatively. It is, however, important to note that the responses depend strongly on the parameterization of sub-grid-scale mixing. Thus, further investigation of the mixing processes and improvements of the parameterization are essential to increase the reliability of simulated iron cycle changes in this region.

In contrast to the simulation results for the higher latitudes, those for low latitudes of the Southern Ocean show a moderate iron input from external iron sources. We found that mixing processes play an important role in supplying iron to surface waters. Because of the continental land masses in the northern part of this region and isopycnals that slope upward toward the south, isopycnal mixing efficiently transports iron to surface waters. Extensive mixed-layer development also contributes to the iron supply to the surface. Because the mixing processes are hardly affected by the simulated future climate changes and the external iron input is fixed in our simulation, our model projected that the surface iron budget change would be small in this region.

The most prominent change that we observed in low latitudes of the Southern Ocean was in horizontal advection, because the spinup and southward shift of the southern subtropical gyres enables more iron-rich waters to intrude into the iron-limited area via the western boundary currents. Recent field data show a tendency for the subtropical front to shift southward as the climate warms (Beal et al., 2011, and references therein), and CMIP5 simulations commonly project the spinup and southward shift of the subtropical gyres under future climate conditions (Meijers et al., 2012). Thus, intensification of advective iron transport from the southern subtropical gyres may occur in the future climate. Reducing model biases in simulations of the southern subtropical gyres would make it possible to better quantify the impact of these changes.

In the eastern equatorial Pacific, we found that most iron originates from shelf sediments around Papua New Guinea. Sedimentary iron is entrained by the western boundary current and then transported by the EUC to the eastern part of the region.

BGD
10, 8505–8559, 2013

Previous observational studies have well documented this west-to-east iron transport (Mackey et al., 2002; Ryan et al., 2006; Slemons et al., 2010) and we also briefly describe such transport in our earlier study (Moore et al., 2013). The observational studies suggest that the NGCU plays a major role in this transport, but our model failed to simulate the NGCU because the Vitiaz Strait, the pathway of the NGCU between New Guinea and New Britain Island, is closed in our coarse-resolution model. Instead, a western boundary current flows northward along the eastern coast of New Britain Island and transports sedimentary iron to the EUC. Because our model can reasonably simulate the EUC (Danabasoglu et al., 2012), the simulated iron transport processes seem realistic in this region.

Our model projected a weakening of the SECC under future climate conditions that results in an iron flux convergence east of New Britain Island and intensification of iron transport to the EUC and, thus, to the eastern equatorial Pacific. Consistent with our results, the multimodel ensemble of CMIP3 simulations has also projected substantial weakening of the SECC (Ganachaud et al., 2012). Consequently, it is likely that future ocean circulation changes will elevate the iron supply to surface waters of the eastern equatorial Pacific. Our model, however, overestimates the extent of the iron-limited area in the equatorial Pacific (Moore et al., 2013); thus, it may also have overestimated the projected increase of production.

In the Subarctic North Pacific, the simulated results showed that HNLC surface waters receive most iron from external sources. Horizontal mixing, which is supported by an advective iron supply by the Kuroshio Current and Alaskan Stream, contributes modestly to the iron supplied to surface waters, and Ekman upwelling in the western subarctic gyre also plays a role. The marginal seas surrounding the Subarctic North Pacific, the Sea of Okhotsk and the Bering Sea, which are not fully resolved in our model, may play an important role in the iron budget in this region (Nishioka et al., 2007; Misumi et al., 2011). Considering the known model bias in simulating iron concentrations in this region (Moore and Braucher, 2008; Misumi et al., 2011), we conclude that the skill of our model in simulating iron cycling in this region is low. We therefore

BGD
10, 8505–8559, 2013

recommend reexamination of iron cycling in this region with models that resolve these marginal seas.

It is usually assumed that stratification of surface waters under a warmer climate will reduce nutrient entrainment from deeper waters. We demonstrated, however, that the surface water iron budget change is not so simple. In the 2090s, the simulated total amount of iron supplied by the net effect of physical processes increases by 13 % in HNLC regions (Table 2). This unexpected response is attributable to the complicated responses of large-scale circulation, including the meridional overturning and gyre circulations, along with the parameterized eddy/convective mixings. Thus, it is essential to improve parameterization of ocean physical processes to obtain better projections of future iron cycle changes. Moreover, although we assumed that the external iron sources would not change in the 21st century, this assumption is not justified. Given that external iron sources have a moderate impact in the low latitudes of the Southern Ocean and in the Subarctic North Pacific, better projections of dust deposition and aerosol iron solubility are important.

4.2 Impact of iron cycle changes on primary and export production rates

An intensified iron supply to HNLC surface waters in the 2090s will likely contribute to elevated primary and export production rates in the HNLC regions. The simulated primary and export production rates integrated over the HNLC regions increase by $1.8\,\mathrm{Gt\,C\,yr^{-1}}$ and $0.15\,\mathrm{Gt\,C\,yr^{-1}}$, respectively, despite the decreased rate of production at a global scale (Table 1). It is important to note, however, that even in HNLC regions, factors other than iron availability, such as improvement of light and temperature conditions under warmer climatic conditions, will also contribute to the elevated production rates (e.g., Steinacher et al., 2010).

To identify the contribution of iron cycle changes to the changes of production, we calculated linear regression slopes and coefficients of determination (R^2) between the simulated temporal changes of iron flux convergence in the upper 100 m accounted for by physical processes and primary and export production rates (Fig. 16). Where

BGD
10, 8505–8559, 2013

the production rates are notably enhanced by the iron supply increase, the regression slopes should be positive, and the R^2 values should be large. Here, we define the IRON-DRIVEN AREA as the area where the regression slopes are positive and R^2 values are 0.5 or more (dotted regions in Fig. 16).

Although the areal extent of the IRON-DRIVEN AREA is not very large, it corresponds to those areas where large changes of production between the 1990s and the 2090s are simulated (Fig. 3b and d). Increases of primary and export production rates integrated over the IRON-DRIVEN AREA are 0.74 Gt C yr^{-1} and 0.08 Gt C yr^{-1}, respectively; thus, in our simulation roughly half of the total changes of production are caused by intensified iron input due to ocean circulation/mixing changes.

A previous ocean biogeochemical model intercomparison study showed that four models, one of which was our previous version (CCSM3), projected decreases in globally integrated primary and export production rates (Steinacher et al., 2010). Among the four models, only CCSM3 projected an increase in production in the eastern equatorial Pacific. This increase of production in the eastern equatorial Pacific is also seen in our CESM1 result (Fig. 3b and d). We demonstrated that the elevated production could be attributed to intensified sedimentary iron transport triggered by weakening of the SECC. Because two of the four models (MPIM and CSM1.4) did not consider sedimentary iron sources, they could not represent this response. The remaining model (IPSL) did consider sedimentary iron sources but nevertheless projected a decrease in production in the eastern equatorial Pacific (Steinacher et al., 2010). We compared simulated dissolved iron distributions of the CESM1 and IPSL models with observed data in the 200–500 m depth range (Fig. 17), where high dissolved iron concentrations have been observed (Slemons et al., 2010). Our model successfully simulated the eastward transport of iron in the equatorial Pacific, whereas the IPSL model did not. Thus, our model response may be more realistic. We acknowledge, however, that our model likely overestimates the increase of production through overestimation of macronutrient concentrations and iron limitation in the equatorial Pacific in the 1990s. Steinacher et al. (2010) predicted that reduced macronutrient entrainment would de-

BGD
10, 8505–8559, 2013

crease production in low-latitude oceans in the future climate. Our results suggest that modest increases in production may be expected in the eastern equatorial Pacific.

5 Conclusions

We investigated the iron budget in the upper ocean during the 1990s and the 2090s by analyzing the simulated results of Community Earth System Model version 1. Although there are some notable biases in the simulated results, comparisons with available field data indicate that the model simulated oceanic circulation and dissolved iron distributions reasonably well. Our results predict that physical transport rather than external iron inputs control most of the surface iron supply in HNLC regions; thus, changes in ocean physical processes and biology in upstream regions would greatly affect the future iron budgets in HNLC surface waters.

Although it is commonly assumed that enhanced stratification in a future warmer climate will reduce nutrient entrainment from deeper waters, we found that intensified meridional overturning and gyre circulations, shifts of their positions, and mixing changes may elevate the iron supply to HNLC surface waters. The simulated oceanic circulation changes in the Southern Ocean and the equatorial Pacific are generally consistent with recent observations under warming climate conditions and other simulated results projected by CMIP3 and CMIP5. Therefore, it is likely that future ocean circulation changes will elevate the iron supply to HNLC surface waters. We also demonstrated that changes in the iron supply due to ocean physical processes will potentially elevate primary and export production rates. Better understanding of the responses of large-scale circulation and mixing processes to a warming climate is essential to make projections of future iron supply changes more robust. Moreover, future work should also consider changes in the distribution, solubility, and amount of aerosol iron deposition.

BGD
10, 8505–8559, 2013

Acknowledgements. The National Center for Atmospheric Research is sponsored by the National Science Foundation. J. K. M. acknowledges the support of NSF grant OCE-0928204. S. C. D. acknowledges support from the National Science Foundation (NSF OPP-0823101 and NSF EF-0424599).

References

Antoine, D., André, J. M., and Morel, A.: Oceanic primary production, 2. Estimation at global scale from satellite (coastal zone color scanner) chlorophyll, Global Biogeochem. Cy., 10, 57–69, 1996.

Archer, D. E. and Johnson, K.: A model of the iron cycle in the ocean, Global Biogeochem. Cy., 14, 269–279, 2000.

Aumont, O., Maier-Reimer, E., Blain, S., and Monfray, P.: An ecosystem model of the global ocean including Fe, Si, P colimitations, Global Biogeochem. Cy., 17, 29–21, 2003.

Beal, L. M., De Ruijter, W. P. M., Biastoch, A., Zahn, R., Cronin, M., Hermes, J., Lutjeharms, J., Quartly, G., Tozuka, T., Baker-Yeboah, S., Bornman, T., Cipollini, P., Dijkstra, H., Hall, I., Park, W., Peeters, F., Penven, P., Ridderinkhof, H., and Zinke, J.: On the role of the Agulhas system in ocean circulation and climate, Nature, 472, 429–436, 2011.

Behrenfeld, M. J. and Falkowski, P. G.: Photosynthetic rates derived from satellite-based chlorophyll concentration, Limnol. Oceanogr., 42, 1–20, 1997.

Behrenfeld, M. J., Boss, E., Siegel, D. A., and Shea, D. M.: Carbon-based ocean productivity and phytoplankton physiology from space, Global Biogeochem. Cy., 19, 1–14, 2005.

Blain, S., Tréguer, P., Belviso, S., Bucciarelli, E., Denis, M., Desabre, S., Fiala, M., Martin Jézéquel, V., Le Fèvre, J., Mayzaud, P., Marty, J. C., and Razouls, S.: A biogeochemical study of the island mass effect in the context of the iron hypothesis: Kerguelen Islands, Southern Ocean, Deep-Sea Res. Pt. I, 48, 163–187, 2001.

Blain, S., Quéguiner, B., Armand, L., Belviso, S., Bombled, B., Bopp, L., Bowie, A., Brunet, C., Brussaard, C., Carlotti, F., Christaki, U., Corbière, A., Durand, I., Ebersbach, F., Fuda, J. L., Garcia, N., Gerringa, L., Griffiths, B., Guigue, C., Guillerm, C., Jacquet, S., Jeandel, C., Laan, P., Lefèvre, D., Lo Monaco, C., Malits, A., Mosseri, J., Obernosterer, I., Park, Y. H., Picheral, M., Pondaven, P., Remenyi, T., Sandroni, V., Sarthou, G., Savoye, N., Scouarnec, L., Souhaut, M., Thuiller, D., Timmermans, K., Trull, T., Uitz, J., Van Beek, P.,

BGD
10, 8505–8559, 2013

Veldhuis, M., Vincent, D., Viollier, E., Vong, L., and Wagener, T.: Effect of natural iron fertilization on carbon sequestration in the Southern Ocean, Nature, 446, 1070–1074, 2007.
Bowie, A. R., Lannuzel, D., Remenyi, T. A., Wagener, T., Lam, P. J., Boyd, P. W., Guieu, C., Townsend, A. T., and Trull, T. W.: Biogeochemical iron budgets of the Southern Ocean south of Australia: decoupling of iron and nutrient cycles in the subantarctic zone by the summertime supply, Global Biogeochem. Cy., 23, GB4034, doi:10.1029/2009GB003500, 2009.
Boyd, P. W. and Ellwood, M. J.: The biogeochemical cycle of iron in the ocean, Nat. Geosci., 3, 675–682, 2010.
Boyd, P. W., Law, C. S., Hutchins, D. A., Abraham, E. R., Croot, P. L., Ellwood, M., Frew, R. D., Hadfield, M., Hall, J., Handy, S., Hare, C., Higgins, J., Hill, P., Hunter, K. A., LeBlanc, K., Maldonado, M. T., McKay, R. M., Mioni, C., Oliver, M., Pickmere, S., Pinkerton, M., Safi, K., Sander, S., Sanudo-Wilhelmy, S. A., Smith, M., Strzepek, R., Tovar-Sanchez, A., and Wilhelm, S. W.: FeCycle: Attempting an iron biogeochemical budget from a mesoscale SF 6 tracer experiment in unperturbed low iron waters, Global Biogeochem. Cy., 19, BG4S20, doi:10.1029/2005GB002494, 2005.
Boyle, E. A., Edmond, J. M., and Sholkovitz, E. R.: The mechanism of iron removal in estuaries, Geochim. Cosmochim. Ac., 41, 1313–1324, 1977.
Coale, K. H., Fitzwater, S. E., Gordon, R. M., Johnson, K. S., and Barber, R. T.: Control of community growth and export production by upwelled iron in the equatorial Pacific Ocean, Nature, 379, 621–624, 1996.
Craig, A. P., Vertenstein, M., and Jacob, R.: A new flexible coupler for earth system modeling developed for CCSM4 and CESM1, Int. J. High Perform. C., 26, 31–42, 2011.
Cunningham, S. A., Alderson, S. G., King, B. A., and Brandon, M. A.: Transport and variability of the Antarctic Circumpolar Current in Drake Passage, J. Geophys. Res.-Oceans, 108, 8084, doi:10.1029/2001JC001147, 2003.
Danabasoglu, G., Ferrari, R., and McWilliams, J. C.: Sensitivity of an ocean general circulation model to a parameterization of near-surface eddy fluxes, J. Climate, 21, 1192–1208, 2008.
Danabasoglu, G., Bates, S. C., Briegleb, B. P., Jayne, S. R., Jochum, M., Large, W. G., Peacock, S., and Yeager, S. G.: The CCSM4 ocean component, J. Climate, 25, 1361–1389, 2012.
de Baar, H. J. W., De Jong, J. R. M., Bakker, D. C. E., Loscher, B. M., Veth, C., Bathmann, U., and Smetacek, V.: Importance of iron for plankton blooms and carbon dioxide drawdown in the Southern Ocean, Nature, 373, 412–415, 1995.

BGD
10, 8505–8559, 2013

Doney, S. C., Lima, I., Feely, R. A., Glover, D. M., Lindsay, K., Mahowald, N., Moore, J. K., and Wanninkhof, R.: Mechanisms governing interannual variability in upper-ocean inorganic carbon system and air–sea CO_2 fluxes: Physical climate and atmospheric dust, Deep-Sea Res. Pt. II, 56, 640–655, 2009a.

Doney, S. C., Lima, I., Moore, J. K., Lindsay, K., Behrenfeld, M. J., Westberry, T. K., Mahowald, N., Glover, D. M., and Takahashi, T.: Skill metrics for confronting global upper ocean ecosystem-biogeochemistry models against field and remote sensing data, J. Marine Syst., 76, 95–112, 2009b.

Duce, R. A. and Tindale, N. W.: Atmospheric transport of iron and its deposition in the ocean, Limnol. Oceanogr., 36, 1715–1726, 1991.

Dufresne, J.-L., Foujols, M.-A., Denvil, S., Caubel, A., Marti, O., Aumont, O., Balkanski, Y., Bekki, S., Bellenger, H., Benshila, R., Bony, S., Bopp, L., Braconnot, P., Brockmann, P., Cadule, P., Cheruy, F., Codron, F., Cozic, A., Cugnet, D., de Noblet, N., Duvel, J.-P., Ethe, C., Fairhead, L., Fichefet, T., Flavoni, S., Friedlingstein, P., Grandpeix, J.-Y., Guez, L., Guilyardi, E., Hauglustaine, D., Hourdin, F., Idelkadi, A., Ghattas, J., Joussaume, S., Kageyama, M., Krinner, G., Labetoulle, S., Lahellec, A., Lefebvre, M.-P., Lefevre, F., Levy, C., Li, Z. X., Lloyd, J., Lott, F., Madec, G., Mancip, M., Marchand, M., Masson, S., Meurdesoif, Y., Mignot, J., Musat, I., Parouty, S., Polcher, J., Rio, C., Schulz, M., Swingedouw, D., Szopa, S., Talandier, C., Terray, P., Viovy, N., and Vuichard, N.: Climate change projections using the IPSL-CM5 Earth System Model: from CMIP3 to CMIP5, Clim. Dynam., 40, 2123–2165, doi:10.1007/s00382-012-1636-1, 2013.

Ellwood, M. J., Boyd, P. W., and Sutton, P.: Winter-time dissolved iron and nutrient distributions in the Subantarctic Zone from 40–52S; 155–160E, Geophys. Res. Lett., 35, L11604, doi:10.1029/2008GL033699, 2008.

Elrod, V. A., Berelson, W. M., Coale, K. H., and Johnson, K. S.: The flux of iron from continental shelf sediments: a missing source for global budgets, Geophys. Res. Lett., 31, L12307 12301–12304, 2004.

Farneti, R., Delworth, T. L., Rosati, A. J., Griffies, S. M., and Zeng, F.: The role of mesoscale eddies in the rectification of the Southern ocean response to climate change, J. Phys. Oceanogr., 40, 1539–1557, 2010.

Ferrari, R., McWilliams, J. C., Canuto, V. M., and Dubovikov, M.: Parameterization of eddy fluxes near oceanic boundaries, J. Climate, 21, 2770–2789, 2008.

BGD
10, 8505–8559, 2013

Fox-Kemper, B., Ferrari, R., and Hallberg, R.: Parameterization of mixed layer eddies, Part I: Theory and diagnosis, J. Phys. Oceanogr., 38, 1145–1165, 2008.
Fox-Kemper, B., Danabasoglu, G., Ferrari, R., Griffies, S. M., Hallberg, R. W., Holland, M. M., Maltrud, M. E., Peacock, S., and Samuels, B. L.: Parameterization of mixed layer eddies, III: Implementation and impact in global ocean climate simulations, Ocean Modell., 39, 61–78, 2011.
Fung, I. Y., Meyn, S. K., Tegen, I., Doney, S. C., John, J. G., and Bishop, J. K. B.: Iron supply and demand in the upper ocean, Global Biogeochem. Cy., 14, 281–295, 2000.
Ganachaud, A., Sen Gupta, A., Brown, J. N., Evans, K., Maes, C., Muir, L. C., and Graham, F. S.: Projected changes in the tropical Pacific Ocean of importance to tuna fisheries, Climatic Change, 1–17, 2012.
Gent, P. R. and Danabasoglu, G.: Response to increasing Southern Hemisphere winds in CCSM4, J. Climate, 24, 4992–4998, 2011.
Gent, P. R. and McWilliams, J. C.: Isopycnal mixing in ocean circulation models, J. Phys. Oceanogr., 20, 150–155, 1990.
Gent, P. R., Danabasoglu, G., Donner, L. J., Holland, M. M., Hunke, E. C., Jayne, S. R., Lawrence, D. M., Neale, R. B., Rasch, P. J., Vertenstein, M., Worley, P. H., Yang, Z. L., and Zhang, M.: The community climate system model version 4, J. Climate, 24, 4973–4991, 2011.
Ginoux, P., Chin, M., Tegen, I., Prospero, J. M., Holben, B., Dubovik, O., and Lin, S. J.: Sources and distributions of dust aerosols simulated with the GOCART model, J. Geophys. Res.-Atmos., 106, 20255–20273, 2001.
Hallberg, R., and Gnanadesikan, A.: The role of Eddies in determining the structure and response of the wind-driven Southern Hemisphere overturning: results from the Modeling Eddies in the Southern Ocean (MESO) project, J. Phys. Oceanogr., 36, 2232–2252, 2006.
Hasumi, H., Tatebe, H., Kawasaki, T., Kurogi, M., and Sakamoto, T. T.: Progress of North Pacific modeling over the past decade, Deep-Sea Res. Pt. II, 57, 1188–1200, 2010.
Hogg, A. M., Meredith, M. P., Blundel, J. R., and Wilson, C.: Eddy heat flux in the Southern Ocean: response to variable wind forcing, J. Climate, 21, 608–620, 2008.
Holland, M. M., Bailey, D. A., Briegleb, B. P., Light, B., and Hunke, E.: Improved sea ice shortwave radiation physics in CCSM4: the impact of melt ponds and aerosols on Arctic sea ice, J. Climate, 25, 1413–1430, 2012.

BGD
10, 8505–8559, 2013

Hunke, E. C. and Lipscomb, W. H.: CICE: The Los Alamos sea ice model user's manual, version 4, 2008.
Hurrell, J. W., Holland, M. M., Ghan, S., Lamarque, J. F., Lawrence, D. M., Lipscomb, W. H., Mahowald, N. M., Marsh, D., Rasch, P. J., Bader, D., Collins, W. D., Gent, P. R., Hack, J. J., Kiehl, J., Kushner, P., Large, W. G., Marshall, S., Vavrus, S., and Vertenstein, M.: The Community Earth System Model: a framework for collaborative research, B. Am. Meteorol. Soc., in press, doi:10.1175/BAMS-D-12-00121, 2013.
Imawaki, S., Uchida, H., Ichikawa, H., Fukasawa, M., and Umatani, S. I.: Satellite altimeter monitoring the Kuroshio transport South of Japan, Geophys. Res. Lett., 28, 17–20, 2001.
Jickells, T. D., An, Z. S., Andersen, K. K., Baker, A. R., Bergametti, C., Brooks, N., Cao, J. J., Boyd, P. W., Duce, R. A., Hunter, K. A., Kawahata, H., Kubilay, N., LaRoche, J., Liss, P. S., Mahowald, N., Prospero, J. M., Ridgwell, A. J., Tegen, I., and Torres, R.: Global iron connections between desert dust, ocean biogeochemistry, and climate, Science, 308, 67–71, 2005.
Johnson, K. S., Chavez, F. P., and Friederich, G. E.: Continental-shelf sediment as a primary source of iron for coastal phytoplankton, Nature, 398, 697–700, 1999.
Kahru, M., Mitchell, B. G., Gille, S. T., Hewes, C. D., and Holm-Hansen, O.: Eddies enhance biological production in the Weddell-Scotia confluence of the Southern Ocean, Geophys. Res. Lett., 34, L14603, doi:10.1029/2007GL030430, 2007.
Kaupp, L. J., Measures, C. I., Selph, K. E., and Mackenzie, F. T.: The distribution of dissolved Fe and Al in the upper waters of the Eastern Equatorial Pacific, Deep-Sea Res. Pt. II, 58, 296–310, 2011.
Klunder, M. B., Laan, P., Middag, R., De Baar, H. J. W., and van Ooijen, J. C.: Dissolved iron in the Southern Ocean (Atlantic sector), Deep-Sea Res. Pt. II, 58, 2678–2694, 2011.
Lam, P. J. and Bishop, J. K. B.: The continental margin is a key source of iron to the HNLC North Pacific Ocean, Geophys. Res. Lett., 35, L07608, doi:10.1029/2008GL033294, 2008.
Lam, P. J., Bishop, J. K. B., Henning, C. C., Marcus, M. A., Waychunas, G. A., and Fung, I. Y.: Wintertime phytoplankton bloom in the subarctic Pacific supported by continental margin iron, Global Biogeochem. Cy., 20, GB1006, doi:10.1029/2005GB002557, 2006.
Lancelot, C., de Montety, A., Goosse, H., Becquevort, S., Schoemann, V., Pasquer, B., and Vancoppenolle, M.: Spatial distribution of the iron supply to phytoplankton in the Southern Ocean: a model study, Biogeosciences, 6, 2861–2878, doi:10.5194/bg-6-2861-2009, 2009.

BGD
10, 8505–8559, 2013

Lannuzel, D., Schoemann, V., de Jong, J., Chou, L., Delille, B., Becquevort, S., and Tison, J. L.: Iron study during a time series in the western Weddell pack ice, Marine Chemistry, 108, 85–95, 2008.

Large, W. G. and Danabasoglu, G.: Attribution and impacts of upper-ocean biases in CCSM3, J. Climate, 19, 2325–2346, 2006.

Lawrence, D. M., Oleson, K. W., Flanner, M. G., Fletcher, C. G., Lawrence, P. J., Levis, S., Swenson, S. C., and Bonan, G. B.: The CCSM4 land simulation, 1850–2005: assessment of surface climate and new capabilities, J. Climate, 25, 2240–2260, 2012.

Lindsay, K., Bonan, G. B., Doney, S. C., Hoffman, F. M., Lawrence, D. M., Long, M. C., Mahowald, N. M., Moore, J. K., Randerson, J. T., and Thornton, P. E.: Preindustrial control and 20th century carbon cycle experiments with the Earth System Model CESM1-(BGC), J. Climate, in review, 2013.

Liu, X. and Millero, F. J.: The solubility of iron hydroxide in sodium chloride solutions, Geochim. Cosmochim. Ac., 63, 3487–3497, 1999.

Long, M. C., Lindsay, K., Peacock, S., Moore, J. K., and Doney, S. C.: 20th century oceanic carbon uptake and storage in CESM1-BGC, J. Climate, in review, 2013.

Longhurst, A., Sathyendranath, S., Platt, T., and Caverhill, C.: An estimate of global primary production in the ocean from satellite radiometer data, J. Plankton Res., 17, 1245–1271, 1995.

Luo, C., Mahowald, N. M., and del Corral, J.: Sensitivity study of meteorological parameters on mineral aerosol mobilization, transport, and distribution, J. Geophys. Res.-Atmos., 108, 4447, doi:10.1029/2003JD003483, 2003.

Mackey, D. J., O'Sullivan, J. E. O., and Watson, R. J.: Iron in the western Pacific: a riverine or hydrothermal source for iron in the Equatorial Undercurrent?, Deep-Sea Res. Pt. I, 49, 877–893, 2002.

Mahowald, N. M. and Luo, C.: A less dusty future?, Geophys. Res. Lett., 30, 1903, doi:10.1029/2003GL017880, 2003.

Mahowald, N., Kohfeld, K., Hansson, M., Balkanski, Y., Harrison, S. P., Prentice, I. C., Schulz, M., and Rodhe, H.: Dust sources and deposition during the last glacial maximum and current climate: a comparison of model results with paleodata from ice cores and marine sediments, J. Geophys. Res.-Atmos., 104, 15895–15916, 1999.

Marshall, G. J.: Trends in the Southern Annular Mode from observations and reanalyses, J. Climate, 16, 4134–4143, 2003.

BGD
10, 8505–8559, 2013

Martin, J. H. and Fitzwater, S. E.: Iron deficiency limits phytoplankton growth in the north-east pacific subarctic, Nature, 331, 341–343, 1988.

Martin, J. H., Gordon, R. M., and Fitzwater, S. E.: Iron in Antarctic waters, Nature, 345, 156–158, 1990.

Martin, J. H., Coale, K. H., Johnson, K. S., Fitzwater, S. E., Gordon, R. M., Tanner, S. J., Hunter, C. N., Elrod, V. A., Nowickl, J. L., Coley, T. L., Barber, R. T., Lindley, S., Watson, A. J., Van Scoy, K., Law, C. S., Liddicoat, M. I., Ling, R., Stanton, T., Stockel, J., Collins, C., Anderson, A., Bidigare, R., Ondrusek, M., Latasa, M., Millero, F. J., Lee, K., Yao, W., Zhang, J. Z., Friederich, G., Sakamoto, C., Chavez, F., Buck, K., Kolber, Z., Greene, R., Falkowski, P., Chisholm, S. W., Hoge, F., Swift, R., Yungel, J., Turner, S., Nightingale, P., Hatton, A., Liss, P., and Tindale, N. W.: Testing the iron hypothesis in ecosystems of the equatorial Pacific Ocean, Nature, 371, 123–129, 1994.

Meehl, G. A., Stocker, T. F., Collins, W. D., Friedlingstein, P., Gaye, A. T. M. G. J., Kitoh, A., Knutti, R., Murphy, J. M., Noda, A., Raper, S. C. B., Watterson, I. G., Weaver, A. J., and Zhao, Z.-C.: Global climate projections, in: Climate Change 2007: The Physical Science Basis, Contribution of Working Group I to the Fourth Assessment Report of the Intergovernmental Panel on Climate Change, edited by: Solomon, S., Qin, D., Manning, M. R., Chen, Z., Marquis, M., Averyt, K. B., Tignor, M., and Miller, H. L., Cambridge University Press, Cambridge, UK and New York, NY, USA, 996 pp., 2007.

Meehl, G. A., Washington, W. M., Arblaster, J. M., Hu, A., Teng, H., Tebaldi, C., Sanderson, B. N., Lamarque, J. F., Conley, A., Strand, W. G., and White, J. B.: Climate system response to external forcings and climate change projections in CCSM4, J. Climate, 25, 3661–3683, 2012.

Meijers, A. J. S., Shuckburgh, E., Bruneau, N., Sallee, J. B., Bracegirdle, T. J., and Wang, Z.: Representation of the Antarctic Circumpolar Current in the CMIP5 climate models and future changes under warming scenarios, J. Geophys. Res.-Oceans, 117, C12008, doi:10.1029/2012JC008412, 2012.

Menard, H. W. and Smith, S. M.: Hypsometry of Ocean Basin Provinces, J. Geophys. Res., 71, 4305–4325, 1966.

Meredith, M. P. and Hogg, A. M.: Circumpolar response of Southern Ocean eddy activity to a change in the Southern Annular Mode, Geophys. Res. Lett., 33, L16608, doi:10.1029/2006GL026499, 2006.

BGD
10, 8505–8559, 2013

Misumi, K., Tsumune, D., Yoshida, Y., Uchimoto, K., Nakamura, T., Nishioka, J., Mitsudera, H., Bryan, F. O., Lindsay, K., Moore, J. K., and Doney, S. C.: Mechanisms controlling dissolved iron distribution in the North Pacific: a model study, J. Geophys. Res.-Biogeo., 116, G03005, doi:10.1029/2010JG001541, 2011.

Misumi, K., Lindsay, K., Moore, J. K., Doney, S. C., Tsumune, D., and Yoshida, Y.: Humic substances may control dissolved iron distribution in the global ocean: implications from numerical simulations, Global Biogeochem. Cy., in press, doi:10.1002/gbc.20039, 2013.

Moore, J. K. and Braucher, O.: Sedimentary and mineral dust sources of dissolved iron to the world ocean, Biogeosciences, 5, 631–656, 2008, http://www.biogeosciences.net/5/631/2008/.

Moore, J. K., Doney, S. C., and Lindsay, K.: Upper ocean ecosystem dynamics and iron cycling in a global three-dimensional model, Global Biogeochem. Cy., 18, 1–21, 2004.

Moore, J. K., Lindsay, K., Doney, S. C., Long, M. C., and Misumi, K.: Marine ecosystem dynamics and biogeochemical cycling in the Community Earth System Model (CESM1-BGC), J. Climate, in review, 2013.

Moss, R. H., Edmonds, J. A., Hibbard, K. A., Manning, M. R., Rose, S. K., Van Vuuren, D. P., Carter, T. R., Emori, S., Kainuma, M., Kram, T., Meehl, G. A., Mitchell, J. F. B., Nakicenovic, N., Riahi, K., Smith, S. J., Stouffer, R. J., Thomson, A. M., Weyant, J. P., and Wilbanks, T. J.: The next generation of scenarios for climate change research and assessment, Nature, 463, 747–756, 2010.

Neale, R. B., Richter, J., Park, S., Lauritzen, P. H., Vavrus, S. J., Rasch, P. J., and Zhang, M.: The mean climate of the Community Atmospheric Model (CAM4) in forced SST and fully coupled experiments, J. Climate, in press, doi:10.1175/JCLI-D-12-00236.1, 2013.

Nishioka, J., Ono, T., Saito, H., Nakatsuka, T., Takeda, S., Yoshimura, T., Suzuki, K., Kuma, K., Nakabayashi, S., Tsumune, D., Mitsudera, H., Johnson, W. K., and Tsuda, A.: Iron supply to the western subarctic Pacific: Importance of iron export from the Sea of Okhotsk, J. Geophys. Res.-Oceans, 112, C10012, doi:10.1029/2006JC004055, 2007.

Nishioka, J., Ono, T., Saito, H., Sakaoka, K., and Yoshimura, T.: Oceanic iron supply mechanisms which support the spring diatom bloom in the Oyashio region, western subarctic Pacific, J. Geophys. Res.-Oceans, 116, C02021, doi:10.1029/2010JC006321, 2011.

Nishioka, J., Obata, H., and Tsumune, D.: Evidence of an extensive spread of hydrothermal dissolved iron in the Indian Ocean, Earth Planet. Sc. Lett., 361, 26–33, 2013.

BGD
10, 8505–8559, 2013

Ryan, J. P., Ueki, I., Chao, Y., Zhang, H., Polito, P. S., and Chavez, F. P.: Western Pacific modulation of large phytoplankton blooms in the central and eastern equatorial Pacific, J. Geophys. Res.-Biogeo., 111, G02013, doi:10.1029/2005JG000084, 2006.

Sakamoto, T. T., Hasumi, H., Ishii, M., Emori, S., Suzuki, T., Nishimura, T., and Sumi, A.: Responses of the Kuroshio and the Kuroshio extension to global warming in a high-resolution climate model, Geophys. Res. Lett., 32, 1–4, 2005.

Sarmiento, J. L. and Gruber, N.: Ocean biogeochemical dynamics, Princeton University Press, USA, 503 pp., 2006.

Screen, J. A., Gillet, N. P., Stevens, D. P., Marshall, G. J., and Roscoe, H. K.: The role of eddies in the Southern Ocean temperature response to the southern annular mode, J. Climate, 22, 806–818, 2009.

Sedwick, P. N., Bowie, A. R., and Trull, T. W.: Dissolved iron in the Australian sector of the Southern Ocean (CLIVAR SR3 section): meridional and seasonal trends, Deep-Sea Res. Pt. I, 55, 911–925, 2008.

Slemons, L., Gorgues, T., Aumont, O., Menkes, C., and Murray, J. W.: Biogeochemical impact of a model western iron source in the Pacific Equatorial Undercurrent, Deep-Sea Res. Pt. I, 56, 2115–2128, 2009.

Slemons, L. O., Murray, J. W., Resing, J., Paul, B., and Dutrieux, P.: Western Pacific coastal sources of iron, manganese, and aluminum to the Equatorial Undercurrent, Global Biogeochem. Cy., 24, GB3024, doi:10.1029/2009GB003693, 2010.

Smith, Jr., K. L., Robison, B. H., Helly, J. J., Kaufmann, R. S., Ruhl, H. A., Shaw, T. J., Twining, B. S., and Vernet, M.: Free-drifting icebergs: hot spots of chemical and biological enrichment in the Weddell Sea, Science, 317, 478–482, 2007.

Smith, R. S., Jones, P., Briegleb, B. P., Bryan, F. O., Danabasoglu, G., Dennis, J., Dukowicz, J., Eden, C., Fox-Kemper, B., Gent, P. R., Hecht, M., Jayne, S. R., Jochum, M., Large, W. G., Lindsay, K., Maltrud, M. E., Norton, N., Peacock, S., Vertenstein, M., and Yeager, S. G.: The Parallel Ocean Program (POP) reference manual, 2010.

Sokolov, S. and Rintoul, S. R.: On the relationship between fronts of the Antarctic Circumpolar Current and surface chlorophyll concentrations in the Southern Ocean, J. Geophys. Res.-Oceans, 112, C07030, doi:10.1029/2006JC004072, 2007.

Spence, P., Fyfe, J. C., Montenegro, A., and Weaver, A. J.: Southern ocean response to strengthening winds in an eddy-permitting global climate model, J. Climate, 23, 5332–5343, 2010.

BGD
10, 8505–8559, 2013

Steinacher, M., Joos, F., Frölicher, T. L., Bopp, L., Cadule, P., Cocco, V., Doney, S. C., Gehlen, M., Lindsay, K., Moore, J. K., Schneider, B., and Segschneider, J.: Projected 21st century decrease in marine productivity: a multi-model analysis, Biogeosciences, 7, 979–1005, doi:10.5194/bg-7-979-2010, 2010.

Tagliabue, A., Bopp, L., Dutay, J. C., Bowie, A. R., Chever, F., Jean-Baptiste, P., Bucciarelli, E., Lannuzel, D., Remenyi, T., Sarthou, G., Aumont, O., Gehlen, M., and Jeandel, C.: Hydrothermal contribution to the oceanic dissolved iron inventory, Nat. Geosci., 3, 252–256, 2010.

Tagliabue, A., Mtshali, T., Aumont, O., Bowie, A. R., Klunder, M. B., Roychoudhury, A. N., and Swart, S.: A global compilation of dissolved iron measurements: focus on distributions and processes in the Southern Ocean, Biogeosciences, 9, 2333–2349, doi:10.5194/bg-9-2333-2012, 2012.

Talley, L. D. and Nagata, Y.: The Okhotsk Sea and Oyashio region, PICES Scientific report No. 2, 227 pp., edited by: Talley, L. D. and Nagata, Y., ISBN 0-9698420-2-3, ISSN 1198-273X., 1995.

Tegen, I. and Fung, I.: Modeling of mineral dust in the atmosphere: sources, transport, and optical thickness, J. Geophys. Res., 99, 22, 897–822,914, 1994.

Tegen, I., Werner, M., Harrison, S. P., and Kohfeld, K. E.: Relative importance of climate and land use in determining present and future global soil dust emission, Geophys. Res. Lett., 31, 5101–5104, 2004.

van Vuuren, D. P., Edmonds, J., Smith, S. J., Calvin, K. V., Karas, J., Kainuma, M., Nakicenovic, N., Riahi, K., van Ruijven, B. J., Swart, R., and Thomson, A.: What do near-term observations tell us about long-term developments in greenhouse gas emissions?, Climatic Change, 103, 635–642, 2010.

Wetz, M. S., Hales, B., Chase, Z., Wheeler, P. A., and Whitney, M. M.: Riverine input of macronutrients, iron, and organic matter to the coastal ocean off Oregon, USA, during the winter, Limnol. Oceanogr., 51, 2221–2231, 2006.

BGD
10, 8505–8559, 2013

Table 1. Globally integrated primary and export production rates simulated by the model.

	1990s	2090s	2090s–1990s
Primary production ($Gt\,C\,yr^{-1}$)			
Global	56.1	52.9	−3.2
HNLC regions	16.4	18.2	1.8 (0.74*)
Export production ($Gt\,C\,yr^{-1}$)			
Global	8.07	7.00	−1.07
HNLC regions	2.69	2.84	0.15 (0.08*)

* Primary and export production changes integrated over the IRON-DRIVEN AREA.

BGD
10, 8505–8559, 2013

Table 2. Globally integrated dissolved iron budget in the upper 100 m (Gmol yr^{-1}).

	1990s	2090s
Global		
TEND	2.49×10^{-3}	6.91×10^{-2}
PHYS	4.09	3.83
ADVv	0.159	0.596
MIXv	1.48	1.29
MIXn	2.47	1.96
BGC	−44.9	−44.5
FRC	40.8	40.8
aeolian dust	8.29	8.29
sediment	32.5	32.5
HNLC		
TEND	-9.59×10^{-5}	1.74×10^{-2}
PHYS	1.60	1.81
ADV	0.425	0.730
MIX	0.521	0.650
MIXn	0.654	0.427
BGC	−2.33	−2.52
FRC	0.73	0.73

"Global" and "HNLC" represent integration regions for the budget analysis. HNLC regions are defined as iron-limited areas for diatoms in the 1990s (Fig. 5c).
TEND represents the dissolved iron tendency due to physical (PHYS), biogeochemical (BGC), and external forcings (FRC) (see Eq. 1).

BGD
10, 8505–8559, 2013

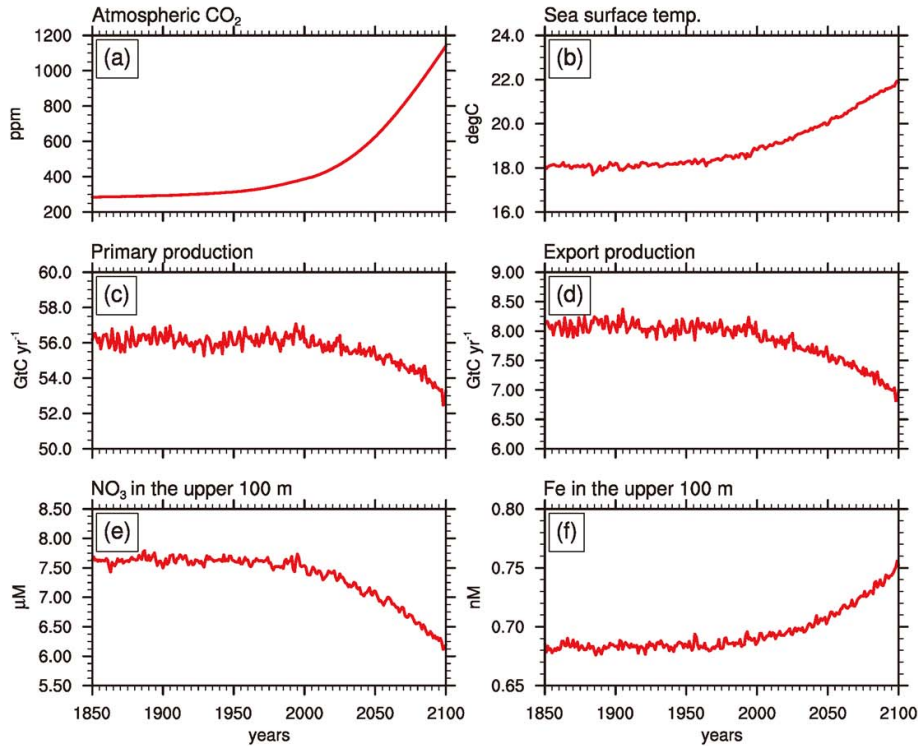

Fig. 1. Temporal variations of **(a)** simulated globally averaged annual mean atmospheric CO_2 (ppm), **(b)** sea surface temperature (°C), **(c)** globally integrated annual mean primary production(Gt C yr^{-1}), **(d)** export production (Gt C yr^{-1}), and **(e)** surface NO_3 (µM) and **(f)** surface Fe (in nM) **(f)** averaged over the upper 100 m.

BGD
10, 8505–8559, 2013

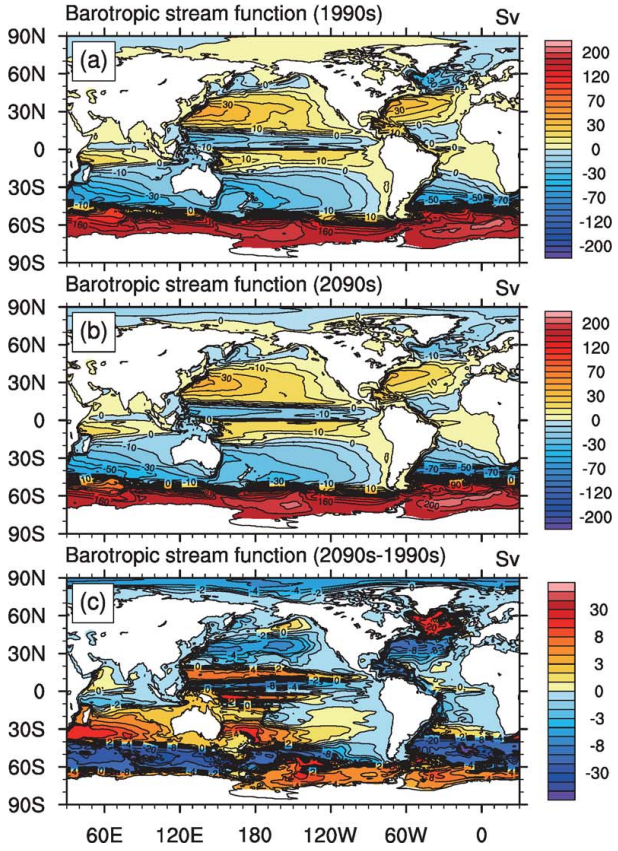

Fig. 2. Spatial distributions of the simulated barotropic (vertically integrated) stream function ($Sv = 10^6\ m^3\ s^{-1}$) in **(a)** the 1990s and **(b)** the 2090s and **(c)** their difference. Positive (negative) values represent clockwise (counterclockwise) circulation.

BGD
10, 8505–8559, 2013

The iron budget in ocean surface waters in the 20th and 21st centuries

K. Misumi et al.

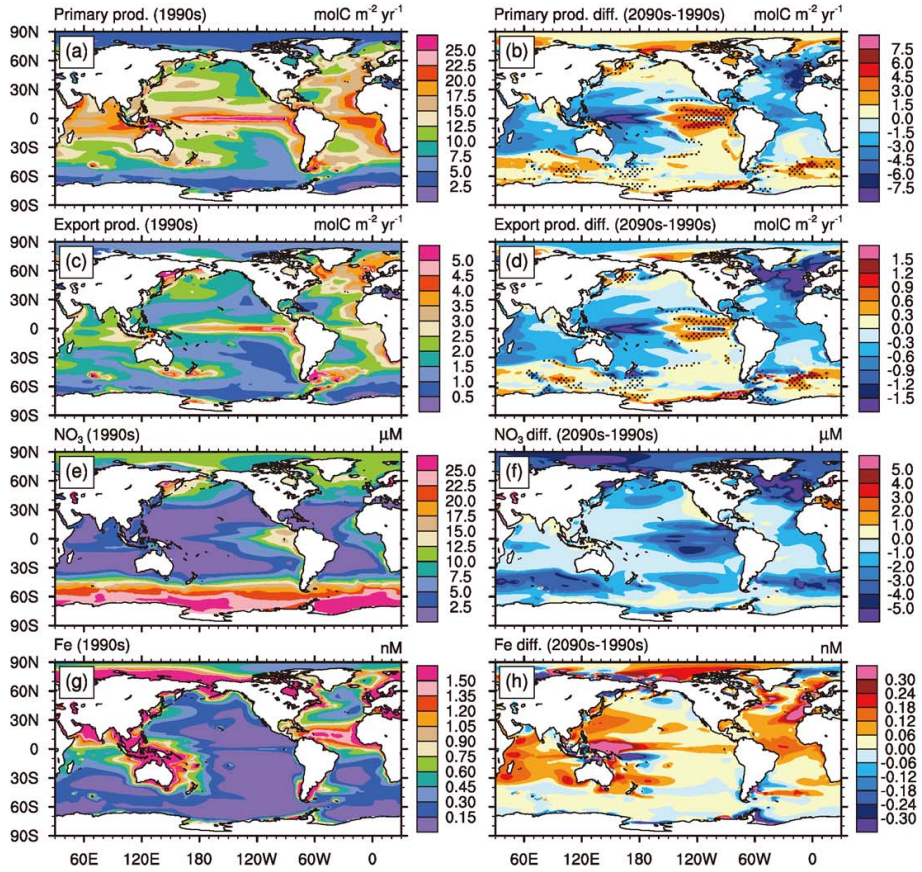

Fig. 3. Spatial distributions of simulated (**a** and **b**) primary production (mg C m^{-2} day^{-1}), (**c** and **d**) export production (mg C m^{-2} day^{-1}), (**e** and **f**) NO_3 (µM) and (**g** and **h**) Fe concentrations (nM) (**a**, **c**, **e** and **g**) in the 1990s and (**b**, **d**, **f** and **h**) their differences between 2090s and 1990s. Dotted regions in panels **(b)** and **(d)** show the IRON-DRIVEN AREA, discussed in Sect. 4.2.

BGD
10, 8505–8559, 2013

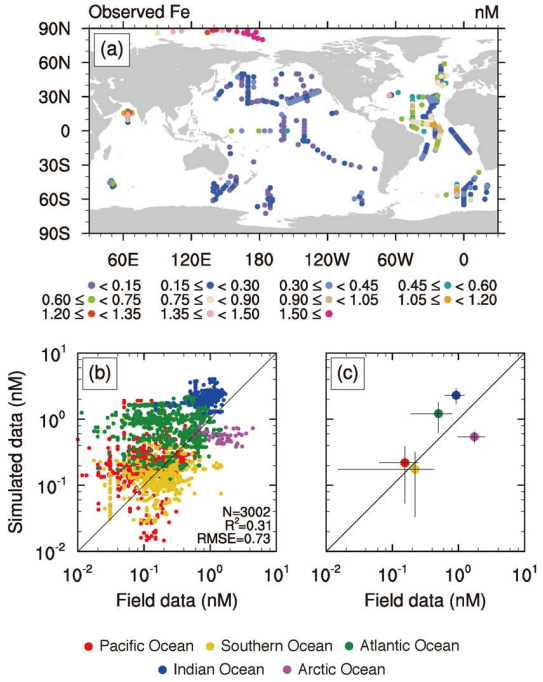

Fig. 4. (a) Spatial distribution of the observed dissolved iron concentration (nM) in the upper 200 m based on data compiled by Tagliabue et al. (2012). (**b** and **c**) Scatter plots comparing the observed data (horizontal axes) with the simulated results in the 1990s (vertical axes) in the upper 200 m. **(b)** The simulated results sub-sampled at the nearest grid points to the measured locations and for the same month. N, number of data; R^2, coefficient of determination; and RMSE, root mean square error. **(c)** The same comparison as in panel **(b)** but showing basin-scale averages. Horizontal and vertical bars represent the standard deviations of the field and simulated data for the individual basins.

BGD
10, 8505–8559, 2013

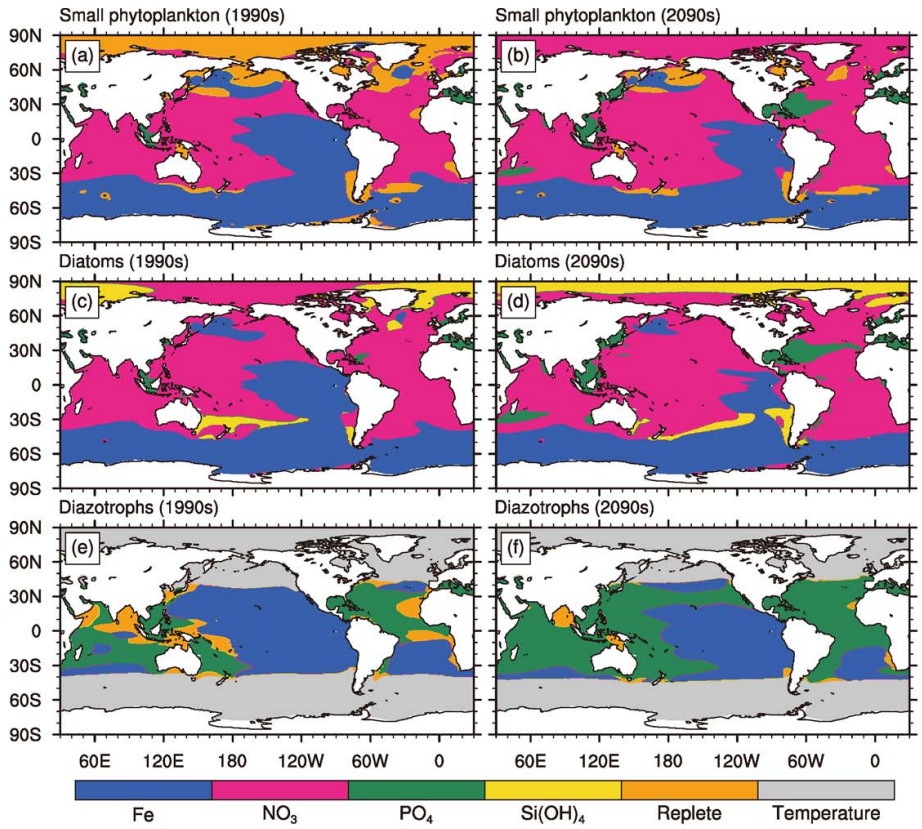

Fig. 5. Spatial distributions of the simulated most limiting factor for phytoplankton growth at an annual timescale during (**a**, **c** and **e**) the 1990s and (**b**, **d** and **f**) the 2090s for small phytoplankton (**a** and **b**), diatoms (**c** and **d**), and diazotrophs (**e** and **f**).

BGD
10, 8505–8559, 2013

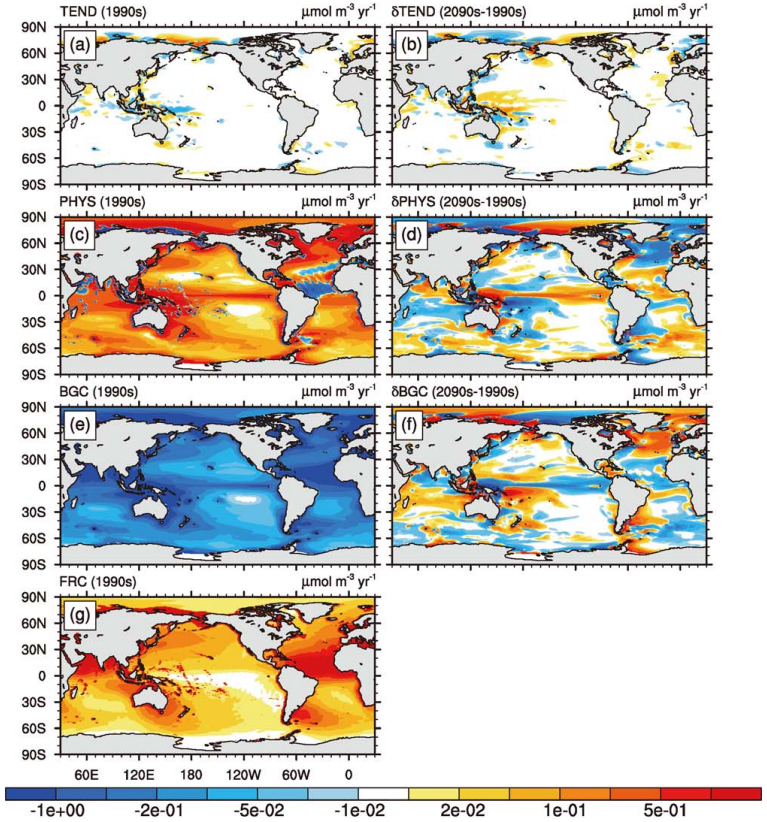

Fig. 6. Spatial distributions of annual-mean dissolved iron tendency (μmol m^{-3} yr^{-1}) averaged over the upper 100 m (**a**, **c**, **e** and **g**) during the 1990s and (**b**, **d** and **f**) the differences between the 2090s and 1990s for the TEND (**a** and **b**), PHYS (**c** and **d**), BGC (**e** and **f**), and FRC **(g)** terms of Eq. (1). Note the logarithmic color scale.

BGD
10, 8505–8559, 2013

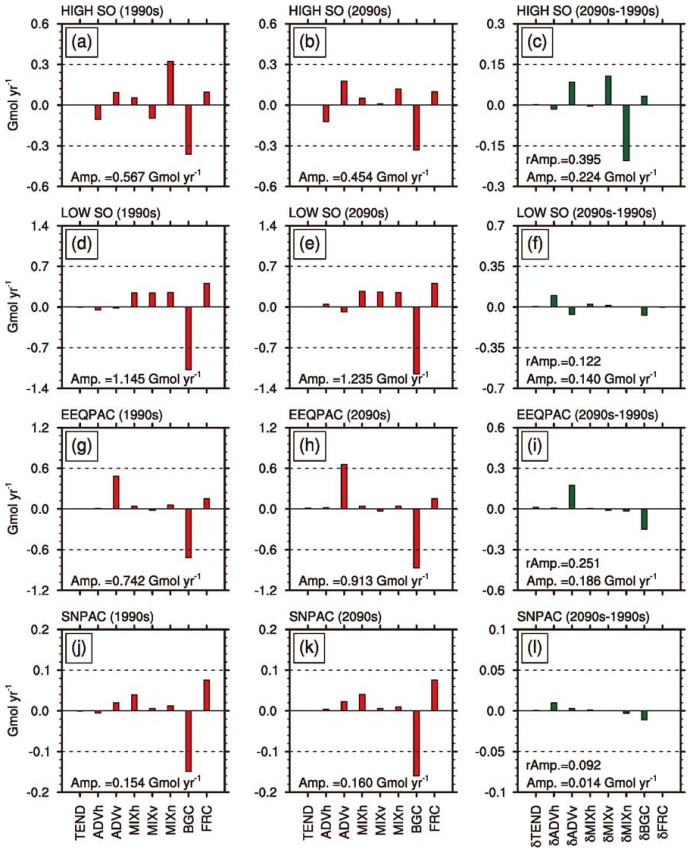

Fig. 7. Regionally integrated dissolved iron tendencies (Gmol yr^{-1}) in the upper 100 m of **(a–c)** HIGH SO, **(d–f)** LOW SO, **(g–i)** EEQPAC, and **(j–l)** SNPAC for (**a**, **d**, **g** and **j**) the 1990s and (**b**, **e**, **h** and **k**) the 2090s and (**c**, **f**, **i** and **l**) the differences between the 2090s and 1990s.

BGD
10, 8505–8559, 2013

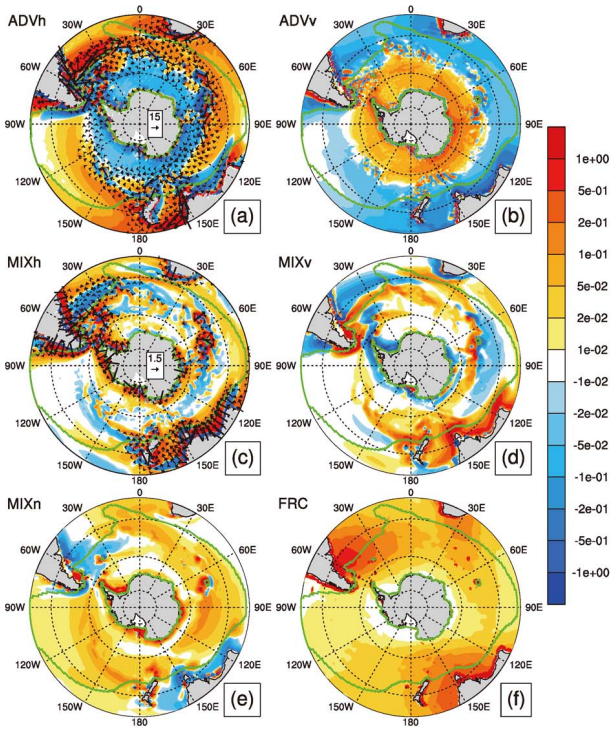

Fig. 8. Spatial distributions of each component of the dissolved iron tendency (color scale, $\mu mol\,m^{-3}\,yr^{-1}$) averaged over the upper 100 m: **(a)** ADVh, **(b)** ADVv, **(c)** MIXh, **(d)** MIXv, **(e)** MIXn, and **(f)** FRC. Vectors represent the horizontal iron flux averaged over the upper 100 m ($mol\,m^{-3}\,yr^{-1}$). The maximum vector length is set to 30 $mol\,m^{-3}\,yr^{-1}$ (3 $mol\,m^{-3}\,yr^{-1}$), and advection (mixing) vectors with magnitudes of less than 3 $mol\,m^{-3}\,yr^{-1}$ (0.3 $mol\,m^{-3}\,yr^{-1}$) are omitted. The green line represents the border of the simulated HNLC region. Dotted concentric circles are the 80° S, 60° S, and 40° S parallels.

BGD
10, 8505–8559, 2013

The iron budget in ocean surface waters in the 20th and 21st centuries

K. Misumi et al.

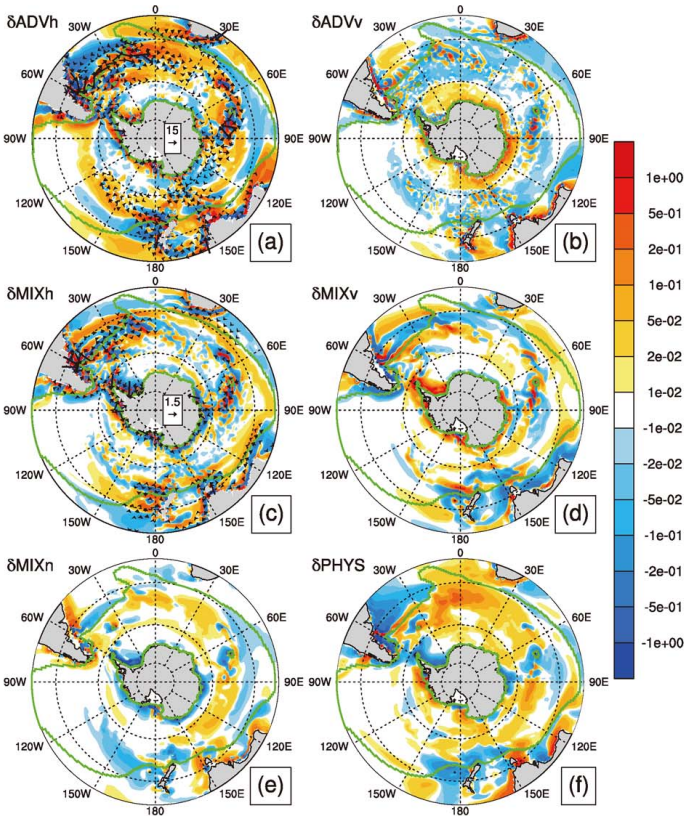

Fig. 9. (a–e) The same as Fig. 8a–e, but for the difference between the 2090s and 1990s. **(f)** The spatial distribution of the δPHYS term (i.e., the sum of **a–e**).

BGD
10, 8505–8559, 2013

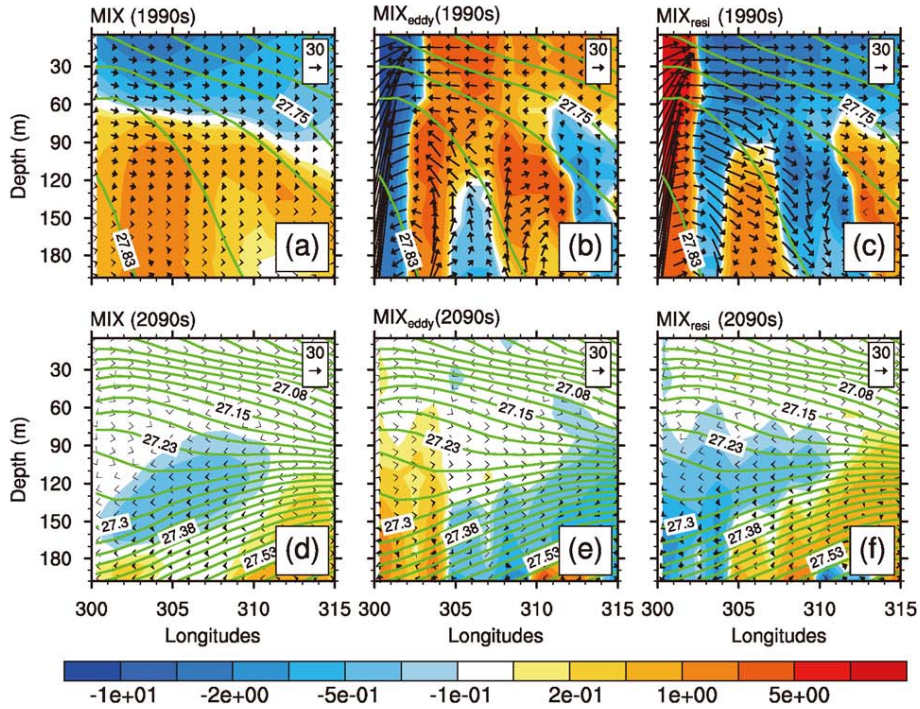

Fig. 10. Zonal cross sections of components of the dissolved iron tendency, (**a** and **d**) MIX, (**b** and **e**) MIX$_{eddy}$, and (**c** and **f**) MIX$_{resi}$ components (see Eq. 8) due east of the Antarctic Peninsula (meridionally averaged over 72.8° S–74.9° S) for **(a–c)** the 1990s and **(d–f)** the 2090s. Colors represent the flux convergence (red) and divergence (blue) of the vertical component only (i.e., MIXv, MIXv$_{eddy}$, and MIXv$_{resi}$; μmol m^{-3} yr^{-1}). Vectors represent the iron fluxes on the x–z section (kmol m^{-3} yr^{-1}). Green contours represent potential density (contour interval, 0.025σ_θ).

BGD
10, 8505–8559, 2013

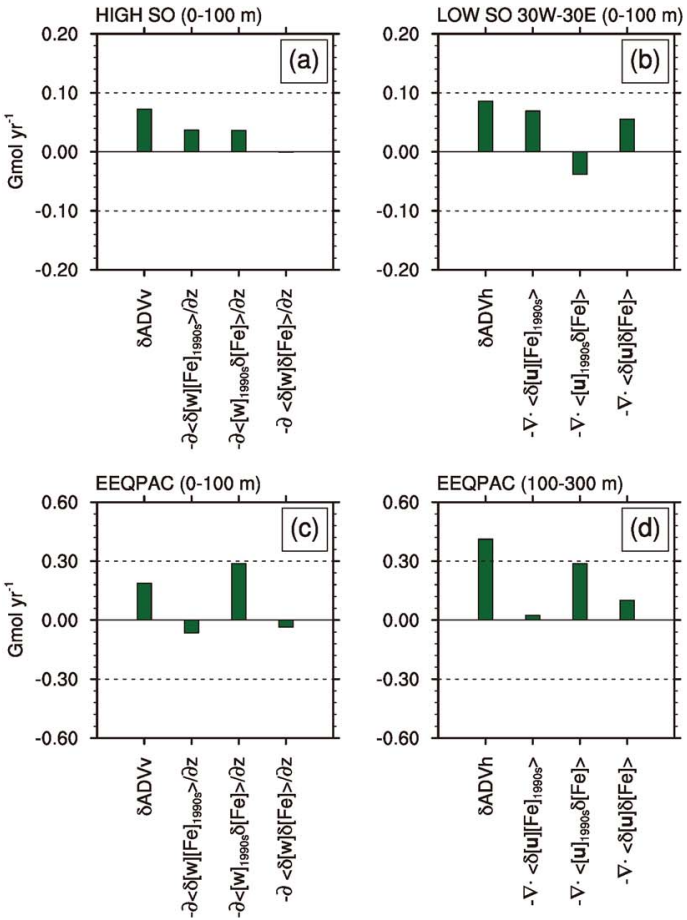

Fig. 11. Decomposition of the δADV term based on Eq. (8) for the upper 100 m in **(a)** HIGH SO, **(b)** LOW SO, and **(c)** EEQPAC. **(d)** The same plot but for the 100–300 m depth range in EEQPAC.

BGD
10, 8505–8559, 2013

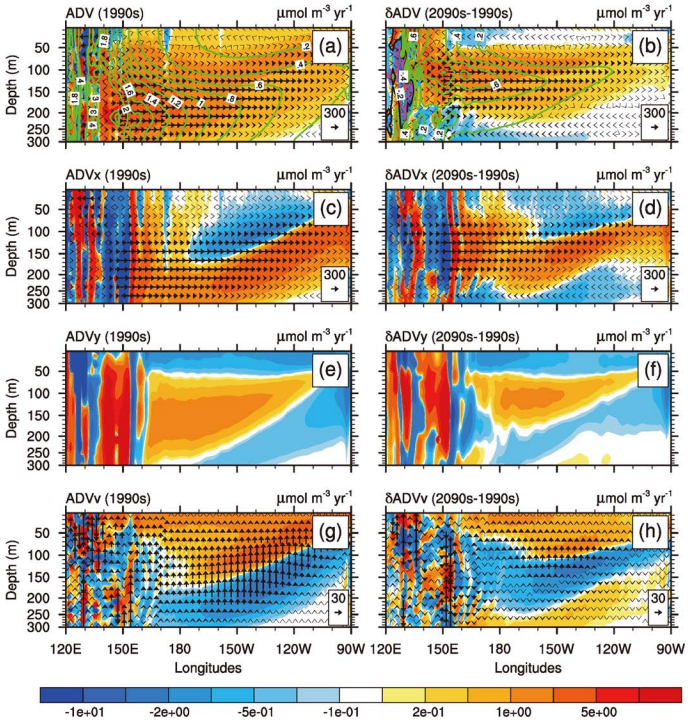

Fig. 12. Zonal cross sections of dissolved iron tendencies ($\mu mol\,m^{-3}\,yr^{-1}$) in the equatorial Pacific (meridionally averaged over 5° S–5° N) for the **(a)** ADV term in the 1990s and **(b)** the δADV term. Vectors represent the iron flux on the x–z section ($kmol\,m^{-3}\,yr^{-1}$). Green, black and magenta contours represent positive, zero, and negative dissolved iron concentrations, respectively. The contour interval is 0.2 nM, except when the absolute value exceeds 2.0 nm the contour interval is 1.0 nM. (**c** and **d**) Zonal, (**e** and **f**) meridional, and (**g** and **h**) vertical components of ADV (1990s) and δADV, respectively.

BGD
10, 8505–8559, 2013

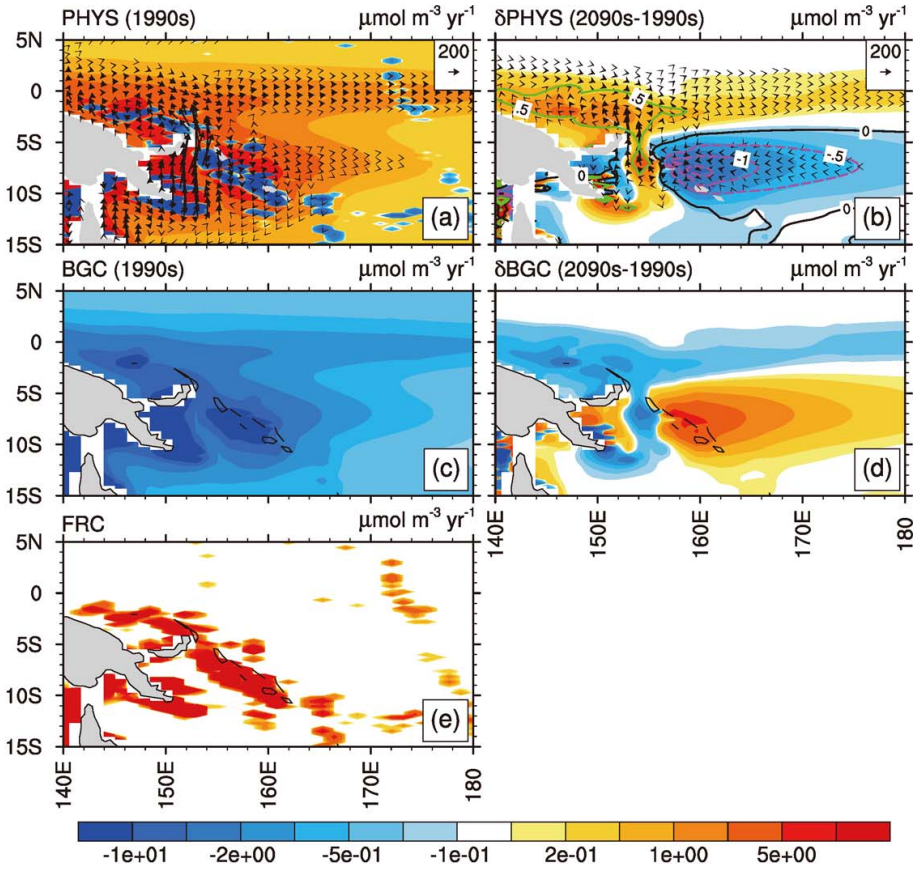

Fig. 13. Spatial distribution of the annual mean dissolved iron tendency ($\mu mol\,m^{-3}\,yr^{-1}$) averaged over the upper 300 m (**a**, **c** and **e**) during the 1990s and (**b** and **d**) the difference between the 2090s and 1990s for (**a** and **b**) the PHYS, (**c** and **d**) BGC, and **(e)** FRC terms of Eq. (1).

BGD
10, 8505–8559, 2013

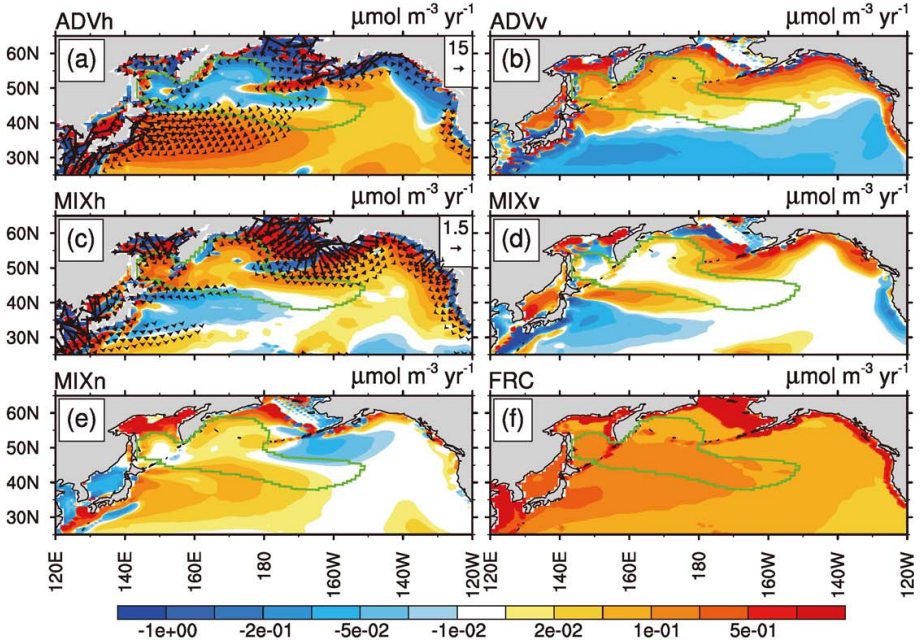

Fig. 14. The same as in Fig. 8 but for the North Pacific.

BGD
10, 8505–8559, 2013

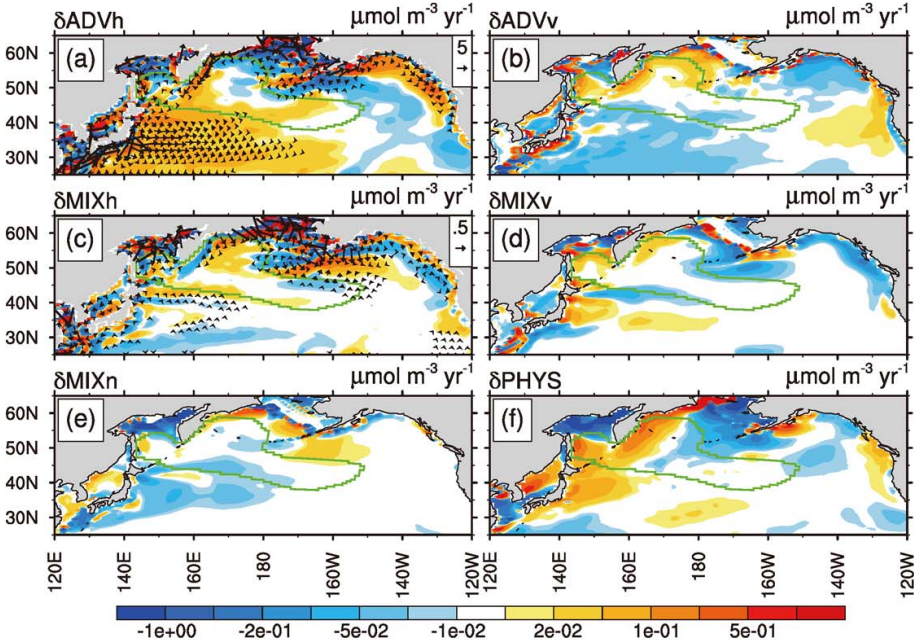

Fig. 15. The same as in Fig. 9 but for North Pacific. The maximum vector length is set to 10 mol m^{-3} yr^{-1} (1 mol m^{-3} yr^{-1}), and advection (mixing) vectors with magnitudes less than 1 mol m^{-3} yr^{-1} (0.1 mol m^{-3} yr^{-1}) are omitted.

BGD
10, 8505–8559, 2013

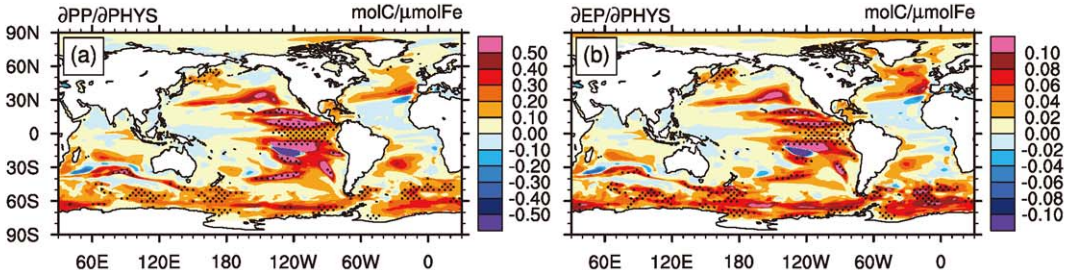

Fig. 16. Spatial distributions of linear regression slopes between **(a)** primary production and **(b)** export production and the dissolved iron supply due to the PHYS term (mol C, µmol Fe^{-1}). The regressions were calculated using the temporal variations of annual means during 1990–2099. Regions with R^2 values exceeding 0.5 are dotted (IRON-DRIVEN AREA, see text).

BGD
10, 8505–8559, 2013

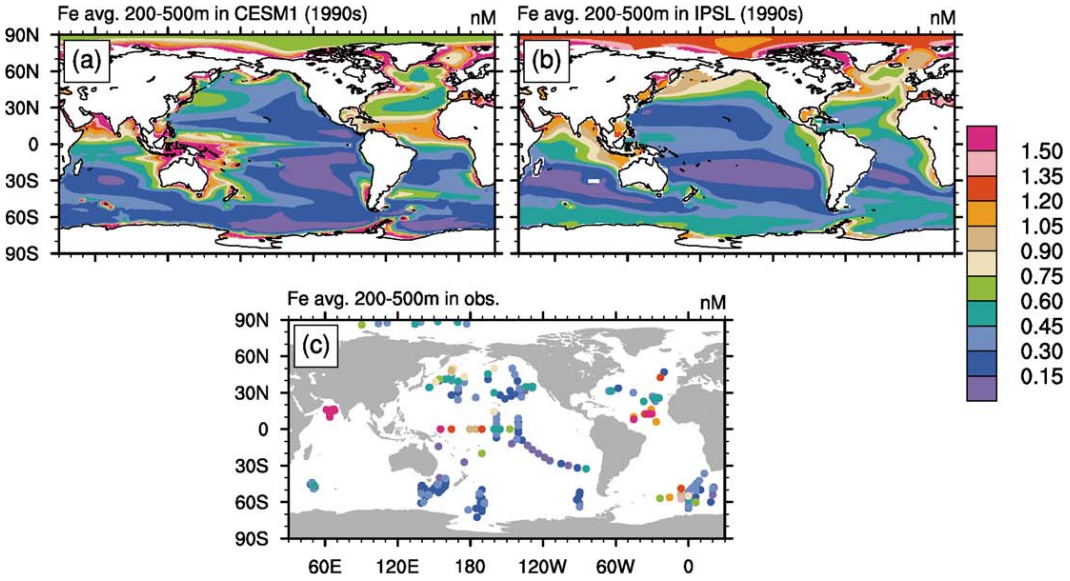

Fig. 17. Dissolved iron concentrations (nM) averaged over the 200–500 m depth interval in the 1990s. Results simulated by **(a)** the CESM1 and **(b)** the IPSL model (downloaded from the CMIP5 archive, http://cmip-pcmdi.llnl.gov/cmip5/; a historical simulation by a model configuration of CM5A-MR; Dufresne et al., 2013). **(c)** Observed data compiled by Tagliabue et al. (2012).

BGD
10, 8505–8559, 2013